FINAL TECHNICAL REPORT

Department of Energy Award Number DE-EE0006086

ACHIEVING TIER 4 EMISSIONS IN BIOMASS COOKSTOVES

Colorado State University

Principal Investigator: Anthony J. Marchese, Ph.D.

CSU Team: Anthony Marchese, Morgan DeFoort, Xinfeng Gao, Jessica Tryner,

Princeton University: Frederick L. Dryer, Francis Haas

Envirofit International: Nathan Lorenz

ACKNOWLEDGMENT

This material is based upon work supported by the Department of Energy's Office of Energy Efficiency and Renewable Energy, Bioenergy Technologies Office, under Award Number EE0006086.

DISCLAIMER

EXECUTIVE SUMMARY

Objectives

Previous literature on top-lit updraft (TLUD) gasifier cookstoves suggested that these stoves have the potential to be the lowest emitting biomass cookstove. However, the previous literature also demonstrated a high degree of variability in TLUD emissions and performance, and a lack of general understanding of the TLUD combustion process. The objective of this study was to improve understanding of the combustion process in TLUD cookstoves. In a TLUD, biomass is gasified and the resulting producer gas is burned in a secondary flame located just above the fuel bed. The goal of this project is to enable the design of a more robust TLUD that consistently meets Tier 4 performance targets through a better understanding of the underlying combustion physics.

The project featured a combined modeling, experimental and product design/development effort comprised of four different activities:

- Development of a model of the gasification process in the biomass fuel bed,
- Development of a CFD model of the secondary combustion zone,
- Experiments with a modular TLUD test bed to provide information on how stove design, fuel properties, and operating mode influence performance and provide data needed to validate the fuel bed model,
- Planar laser-induced fluorescence (PLIF) experiments with a two-dimensional optical test bed to provide insight into the flame dynamics in the secondary combustion zone and data to validate the CFD model
- Design, development and field testing of a market ready TLUD prototype.

Results

Over 180 tests of 40 different configurations of the modular TLUD test bed were performed to demonstrate how stove design, fuel properties and operating mode influences performance, and the conditions under which Tier 4 emissions are obtainable. Images of OH and acetone PLIF were collected at 10 kHz with the optical test bed. The modeling and experimental results informed the design of a TLUD prototype that met Tier 3 to Tier 4 specifications in emissions and Tier 2 in efficiency. The prototype was field tested in India.

INTRODUCTION TO THE PROBLEM

In a top-lit up draft (TLUD) gasifier cookstove (**Figure 1**), the fuel chamber is typically batched-loaded with bed of solid biomass. The fuel bed is then ignited from the top. Primary air flows up through the fuel bed and provides the oxidizer needed to gasify the biomass in the "primary combustion zone". The heat released during partial oxidation of the pyrolysis gases leaving the solid fuel drives the continued pyrolysis of the biomass, and the primary combustion zone progresses downward through the fuel bed. Gases leaving the primary combustion zone pass up through the hot char bed, where they may react further, and mix with secondary air near the top of the stove. The flame that heats the cooking surface is formed in this "secondary combustion zone."[1] Primary and secondary air flows are driven entirely by natural convection in a "natural draft" stove and are assisted by a fan in a "forced-air" stove.

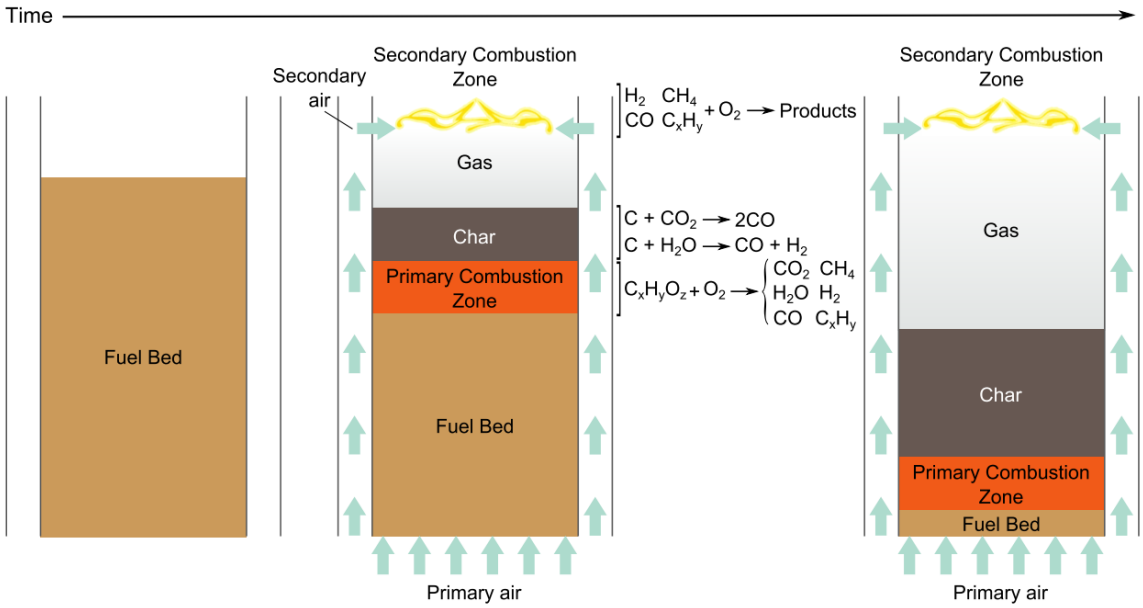

Figure 1. Schematic of top-lit updraft (TLUD) gasifier cookstove operation.[2]

Household biomass gasifier cookstoves have attracted interest due to their demonstrated ability to emit less CO and $PM_{2.5}$ than other cookstove designs in the laboratory[3–5] and in the field.[6–8] Unfortunately, highly variable performance has also been observed among gasifier cookstoves, and some have been found to emit more CO and $PM_{2.5}$ than a three-stone fire.[5] In this study, we investigated the combustion process that takes place inside of gasifier cookstoves in more detail with the goals of: (a) identifying the sources of this variability and (b) enabling development of a gasifier cookstove that could reliably operate with low emissions. We measured emissions from gasifier cookstoves in a laboratory fume hood, applied high-speed combustion diagnostic imaging to a model burner with optical access, and developed a computational fluid dynamic (CFD) model of the secondary combustion zone.

EXPERIMENTAL

Three sets of experiments were conducted. In the first set, five natural draft gasifier cookstove configurations were tested in the laboratory with two different fuel types to identify the sources of variability in gasifier cookstove performance. In the second set of experiments, a modular gasifier cookstove was tested in the laboratory to characterize the manner in which stove design, fuel properties, and operating mode influenced performance. In the third second of experiments, chemiluminescence and planar laser-induced fluorescence (PLIF) images were collected using a two-dimensional model of the secondary combustion zone to: (a) study the effects of secondary air velocity on fuel-air mixing and the flame dynamics and (b) generate a dataset that could be used to validate a CFD model of the secondary combustion zone.

Natural Draft Gasifier Cookstove Testing

As part of the effort to collect baseline gasifier performance data, five configurations of natural draft TLUD gasifier cookstoves (see **Figure 2**) were tested using two fuels (corn cobs and Lodgepole pine pellets) to determine how changes in stove design, fuel type, and operator behavior affected performance in terms of carbon monoxide (CO) emissions, particulate matter (PM_{10}) emissions, and fuel efficiency.

The first configuration ("Stove 1") was a chimney stove in the original form as received from the manufacturer (Shanxi Jinqilin Energy Technology Co. Ltd.). The second and third configurations were modified version of the first. These two configurations were designed to increase the heat transfer efficiency of Stove 1 for the purposes of the study. The fourth stove was the Philips HD4008 and the fifth used the open-source Peko Pe design. These five configurations are referred to as Stoves 1, 2, 3, 4, and 5 below.

Each stove was placed in a fume hood and operated at high power to bring 5 L of water from 15 °C to 90 °C. Carbon monoxide emissions in the fume hood exhaust were measured using an electrochemical sensor; PM_{10} was sampled onto PTFE filters and measured gravimetrically. The mass of biomass fuel consumed and the mass of char produced were measured to quantify thermal efficiency. This test was repeated 2–4 times with each stove/fuel combination.

An energy balance model was developed, using temperature data collected from thermocouples mounted on each configuration, to identify the factors that contributed the most to sub-unity efficiency. This model accounted for the energy transferred to the water in the pot, left over as char, stored in the stove body, lost from the stove body through radiation and convection, and lost through the exhaust.

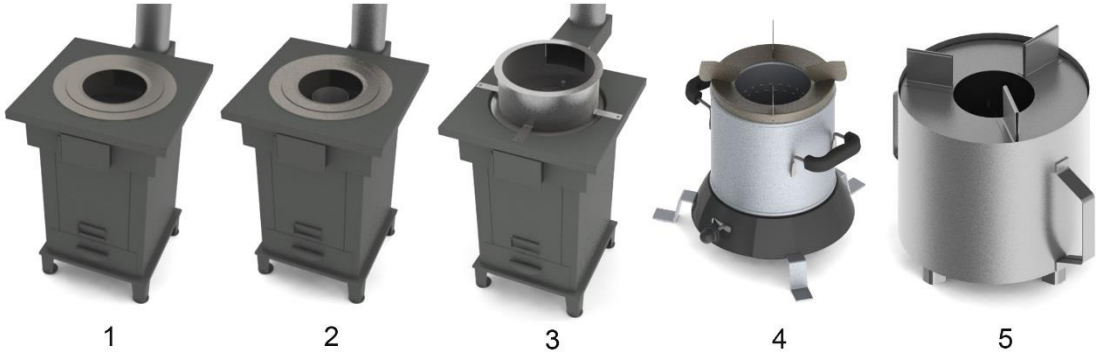

Figure 2. Renderings of the five natural draft gasifier cookstoves tested. Stove 1 (Jinqilin natural draft) was 64 cm tall, weighed 37 kg and was equipped with a chimney. Stoves 2 and 3 were modified versions of Stove 1. Stove 4 (Philips HD4008) was 30 cm in height and weighed 3.6 kg. Stove 5 (Peko Pe) was 25 cm in height and weighed 2.7 kg. Stoves 4 and 5 were not equipped with chimneys.[9]

Stove design, fuel type, and operator behavior all influenced emissions. Four of the five configurations exhibited lower emissions when fueled with wood pellets than when fueled with corn cobs (**Figure 3**). For example, when Stove 5 was fueled with wood pellets instead of corn cobs, CO and PM emissions decreased by factors of 11 and 3. Stove 5 fueled with wood pellets had the lowest emissions (0.6 g $CO \cdot MJ_d^{-1}$ and 48 mg $PM_{10} \cdot MJ_d^{-1}$). These results underscore the need to test stoves with the fuel that the consumer is most likely to use.

The thermal efficiencies of Stoves 1, 2, and 3 were approximately 9%, 12%, and 20%, whereas the efficiencies of Stoves 4 and 5 ranged from 35% to 43% (**Figure 3**). Stoves 1, 2, and 3, which had high thermal masses and a chimney, had more heat addition to the stove body and energy transferred out of the stove via the exhaust gases than Stoves 4 and 5 (**Figure 4**).

CO emissions were high for Stove 1 fueled with corn cobs because the stove had to be refueled twice during the test. Due to the low bulk energy content of the corn cobs and high thermal mass of the stove, the initial fuel bed was consumed before the test was complete. When subsequent batches of fuel were added to the stove, large transient increases in the CO emission rate were observed. Similar trends were observed when Stoves 2 and 3 were fueled with corn cobs; however, because Stoves 2 and 3 exhibited improved heat transfer to the pot, Stove 2 only had to be refueled once and Stove 3 did not have to be refueled at all during the test. The lower overall emissions for Stoves 2 and 3 resulted from reducing the number of

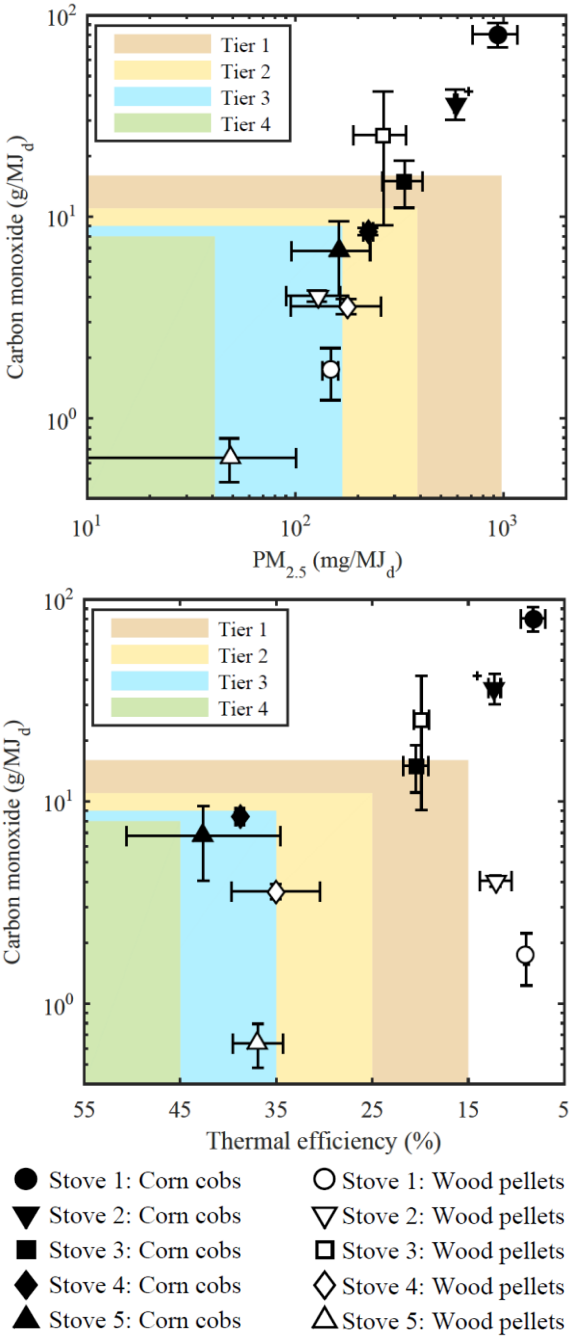

Figure 3. Average high-power CO emissions vs. average high-power PM_{10} emissions (top) and average thermal efficiency (bottom) compared to ISO tiers for biomass stove performance. Error bars represent one standard deviation with the exception of the error bars on the data point for Stove 2 fueled with corn cobs. This data point (marked with a `+') is based on only two test replicates and the error bars represent the total range of the two results.[2]

transient increases in emissions associated with refueling events. Stove 4 had to be refueled once during the test with corn cob fuel; however, a large increase in the CO emission rate was not observed upon refueling. Stove 5 did not require refueling during tests with either fuel.

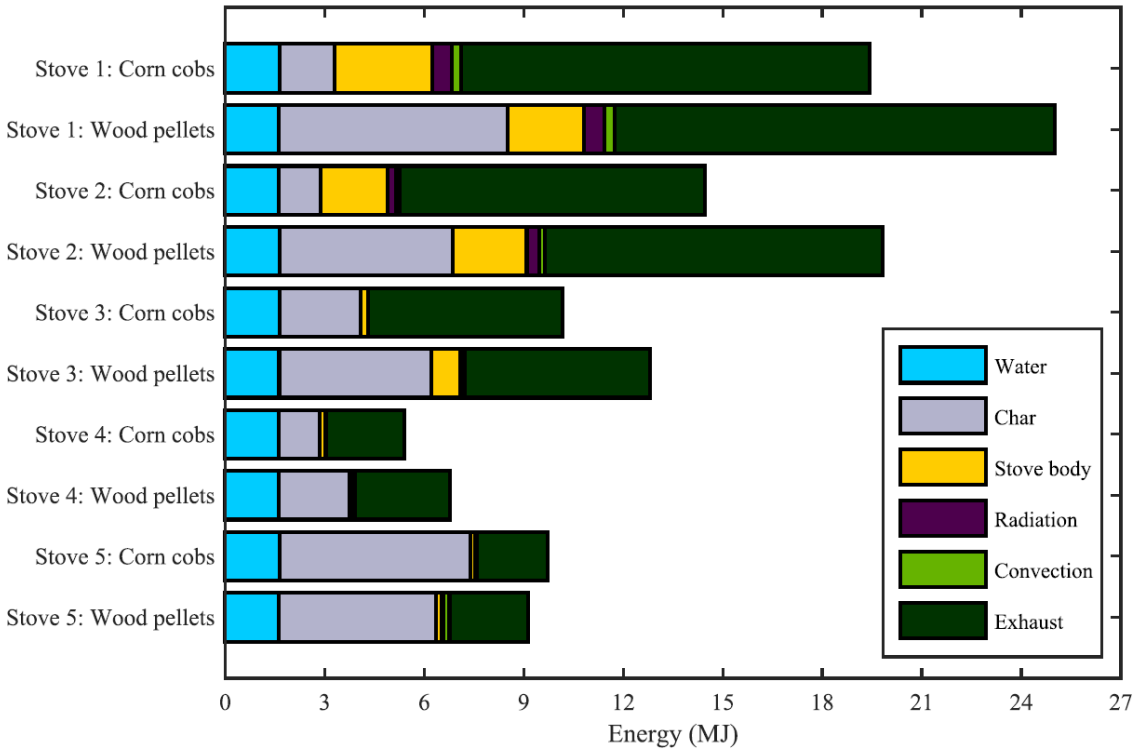

Figure 4. Results of the energy balance with the energy consumption attributed to each component shown. The overall length of the bar for each test case represents the total energy input into the stove, in the form of fuel, to bring 5 L of water from 15 to 90 °C.[2]

Stove 5 consumed more energy than Stove 4 because more of the energy input to Stove 5 was left over as char at the end of the test (**Figure 4**). The average fraction of fuel energy left over as char was 52% for Stove 5 fueled with wood pellets and 59% for Stove 5 fueled with corn cobs. For Stoves 1–4, this fraction ranged from 8% for Stove 1 fueled with corn cobs to 35% for Stove 3 fueled with wood pellets. Whether or not the energy in the char is subtracted from the energy in the fuel consumed can have a large effect on the efficiency value calculated for a gasifier cookstove. For example, the efficiency calculated for Stove 5 fueled with corn cobs was 17% without the char energy subtracted and 43% with the char energy subtracted.

For more information, see the following documents:

- Tryner, J.; Willson, B. D.; Marchese, A. J. The effects of fuel type and stove design on emissions and efficiency of natural-draft semi-gasifier biomass cookstoves. *Energy Sustainable Dev.* **2014**, *23*, 99–109, DOI: 10.1016/j.esd.2014.07.009.
- Tryner, J. Combustion Phenomena in Biomass Gasifier Cookstoves. Ph.D. Dissertation, Colorado State University, Fort Collins, CO, 2016, http://hdl.handle.net/10217/176745.

Modular Gasifier Cookstove Testing

A modular gasifier cookstove (**Figure 5**) was constructed and tested to investigate the impacts of fuel type, moisture content, and bulk density; primary air flow rate; secondary air flow rate, temperature, and inlet geometry; as well as secondary combustion zone geometry on gasifier cookstove performance. Four fuels, 4 fuel moisture contents, 4 primary air flow rates, 4 secondary air flow rates, 5 secondary air temperatures, and 17 different stove geometries were evaluated. The fuels included Lodgepole Pine wood pellets, Douglas Fir wood chips, Eucalpytus wood chips, and corn cobs.

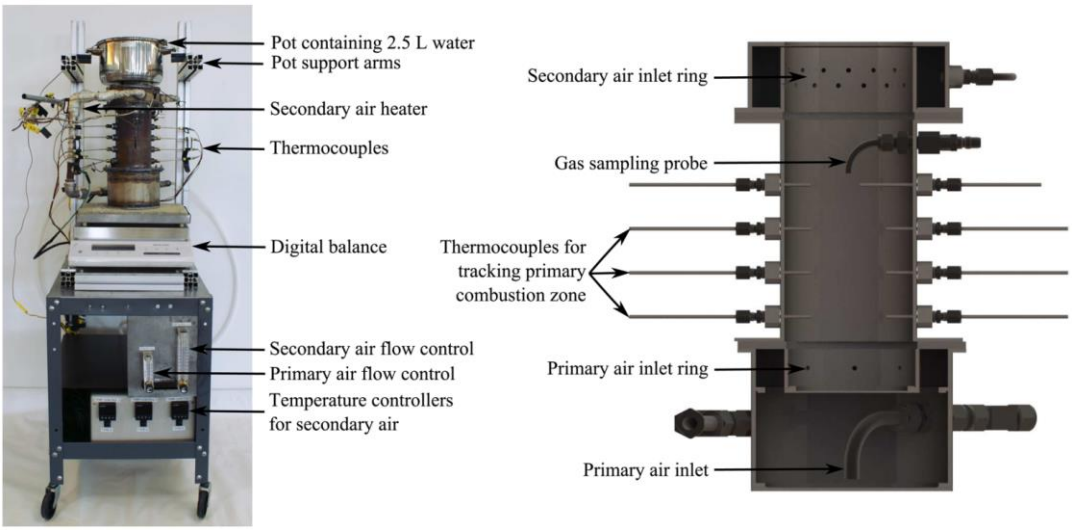

Figure 5. A photograph (left) and cross-sectional view (right) of the modular gasifier cookstove that was used to investigate the impacts of fuel type, fuel moisture content, primary air flow rate, secondary air flow rate, secondary air temperature, and secondary inlet geometry, and secondary combustion zone geometry on gasifier cookstove performance.[10]

Performance of the modular stove was evaluated using a test procedure that was designed to capture normal high-power TLUD operation ("Phase 1"), post-refueling high-power operation ("Phase 2"), and char burnout ("Phase 3"; **Figure 6**). At the start of the test, the empty fuel chamber was filled with fresh biomass fuel and the fuel bed was lit from the top. Emissions were sampled while the stove operated normally at high power to boil 2.5 L of water (Phase 1). After the water temperature reached 90 °C, the PM filter sample was stopped, the pot of water was removed from the stove, and the stove operated normally until the fuel bed completely gasified and the secondary flame extinguished. A second batch of biomass fuel was then added on top of the hot char bed left behind by the first batch of fuel and the secondary flame was re-lit. Post-refueling emissions were sampled while the stove was operated at high power to boil 2.5 L of water (Phase 2). After the water temperature reached 90 °C, the PM filter sample was stopped. The pot of water was removed from the stove briefly, weighed, and returned to the stove. When the second batch of fuel was consumed and the secondary flame extinguished, a third PM filter sample was started and emissions were sampled for 20 minutes while the leftover char burned in the bottom of the fuel chamber (Phase 3).

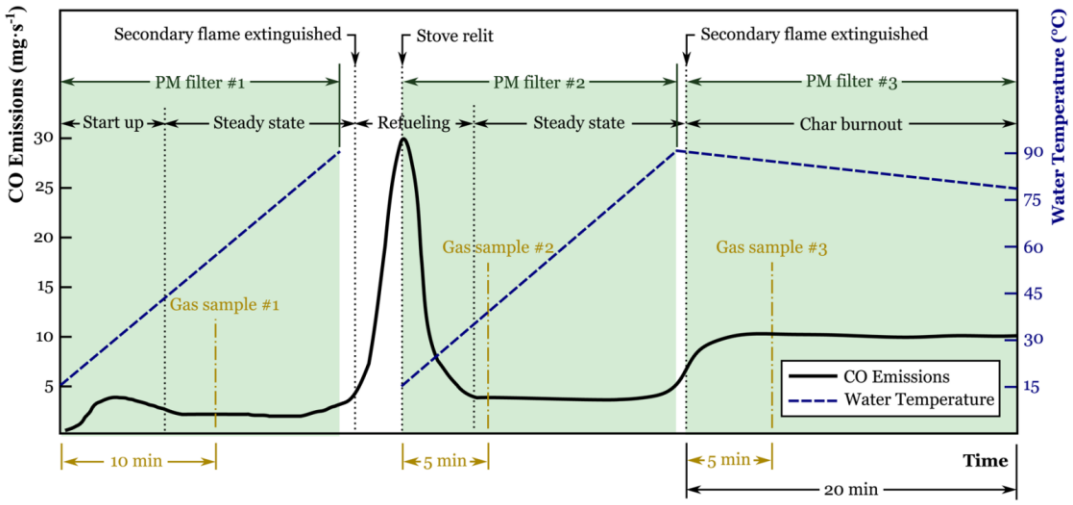

Figure 6. A schematic of the test procedure designed to evaluate performance of the modular stove during normal TLUD operation ("Phase 1"), post-refueling ("Phase 2"), and char burnout ("Phase 3"). The water temperature and CO emissions were monitoring continuously. Gravimetric samples of $PM_{2.5}$ emissions were collected during the time periods shown. Samples of the producer gas entering the secondary combustion zone were collected 10 minutes after the start of Phase 1, 5 minutes after the start of Phase 2, and 5 minutes after the start of Phase 3.[10]

Notable conclusions drawn from these experiments were as follows:

Fuel type: Changes in fuel type sometimes resulted in order-of-magnitude changes in $PM_{2.5}$ emissions (**Figure 7**). Emissions were highest with the corn cob fuel and lowest with Lodgepole Pine pellets (390 vs. 23 mg $PM_{2.5} \cdot MJ_d^{-1}$, on average, during normal operation). The peak fuel bed temperature during normal operation was highest for Lodgepole Pine pellets and lowest for corn cobs, potentially due to the higher bulk energy density of the pellets. The composition of the producer gas entering the secondary combustion zone was also affected by fuel type. Average H_2 concentrations (by volume) were 103% and 23% higher during normal operation and post-refueling when the stove was fueled with Lodgepole Pine pellets instead of Douglas Fir chips. Conversely, average H_2 concentrations were 64% lower during normal operation when the stove was fueled with corn cobs instead of Douglas Fir chips.

Fuel moisture content: The useful power output of the stove decreased linearly as the moisture content (wet basis) of the fuel increased. Variation in fuel moisture content between 0% and 25% did not have a large impact on emissions during normal operation ("Phase 1").

Primary air flow rate: The useful power output of the stove increased linearly as the mass flow rate of primary air increased.

Secondary air flow rate: A minimum in high-power CO emissions was observed for secondary-to-primary air flow ratios of 3:1 and 4:1 (on a mass basis).

Secondary air inlet geometry: Higher secondary air jet velocities resulted in lower emissions, most likely as a result of better fuel-air mixing. Applying a small swirl angle (15°) to the

secondary air jets resulted in no change in high-power CO emissions, whereas larger swirl angles (30° and 45°) resulted in higher emissions, possibly because higher swirl angles increased the residence time in fuel-rich combustion zones.

Operating mode: Total emissions of CO and $PM_{2.5}$ were greater post-refueling (Phase 2) than during normal operation (Phase 1) for all test cases (**Figure 7**). Post-refueling performance was also highly variable. Temperature measurements taken in the fuel bed indicated that gasification of the solid fuel progressed from top of the fuel bed to the bottom during normal operation and from the bottom of the fuel bed to the top after refueling. Concentrations of H_2, CO, and CH_4 in the producer gas entering the secondary combustion zone were highest during normal operation. For example, when the stove was fueled with Douglas Fir wood chips, the average H_2, CO, and CH_4 concentrations in the producer gas were 61%, 36%, and 23% lower post-refueling and 93%, 81%, and 81% lower during char burnout.

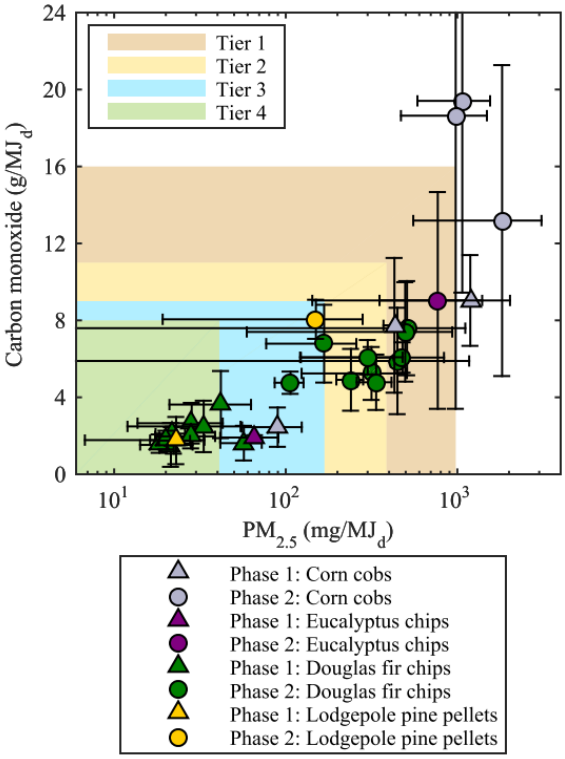

Figure 7. Average high-power CO and $PM_{2.5}$ emissions for tests of varying primary air flow rates, fuel types, fuel moisture contents, fuel bulk densities, and secondary combustion zone geometries. Error bars represent 90% confidence intervals. The 2012 ISO International Workshop Agreement tiers for high-power emissions are also shown.[3]

The lowest high-power emissions measured during normal operation were 1.6 g $CO \cdot MJ_d^{-1}$ (90% confidence interval (CI) = 1.1–2.1) and 18 mg $PM_{2.5} \cdot MJ_d^{-1}$ (90% CI = 17–19) for the stove fueled with Douglas Fir wood chips with a 0% moisture content, a primary air flow rate of 25 $g \cdot min^{-1}$, and primary-to-secondary air flow ratio of 3:1, 200 °C secondary air, and 4-mm-diameter secondary air inlet holes. These values were well below the Tier 4 targets of 8 g $CO \cdot MJ_d^{-1}$ and 41 mg $PM_{2.5} \cdot MJ_d^{-1}$. However, the high-power emissions measured during testing of the modular gasifier stove ranged from Tier 0 to Tier 4 (when compared to the metrics listed in the 2012 ISO International Workshop Agreement[11]) depending on the stove design, fuel type, and operating mode (**Figure 7**). Given the extent to which fuel type and operating mode were demonstrated to influence emissions, it is important to consider the fuels and operator behaviors that are likely to accompany field use when evaluating the performance of a prototype biomass cookstove.

Particle size and number emissions were measured at 1 Hz for the modular stove fueled with Douglas Fir wood chips (7% moisture content), a primary air flow rate of 25 g·min^{-1}, a primary-to-secondary air flow ratio of 3:1, 200 °C secondary air, and 2-mm-diameter secondary air inlets. The measured particle number size distribution was combined with effective density values from the literature to estimate the relative masses of PM emitted during five segments of the test: (1) normal operation with the pot on the stove ("cold start," 0–770 s in **Figure 8**), (2) normal operation with the pot removed (770–1170 s), (3) transient refueling emissions (1170–1390 s), (4) post-refueling steady-state operation (1390–1770 s), and (5) secondary flame extinguished and char burnout ("shut down," 1770–2500 s). These five masses were normalized to the mass emitted during normal operation with the pot on the stove.

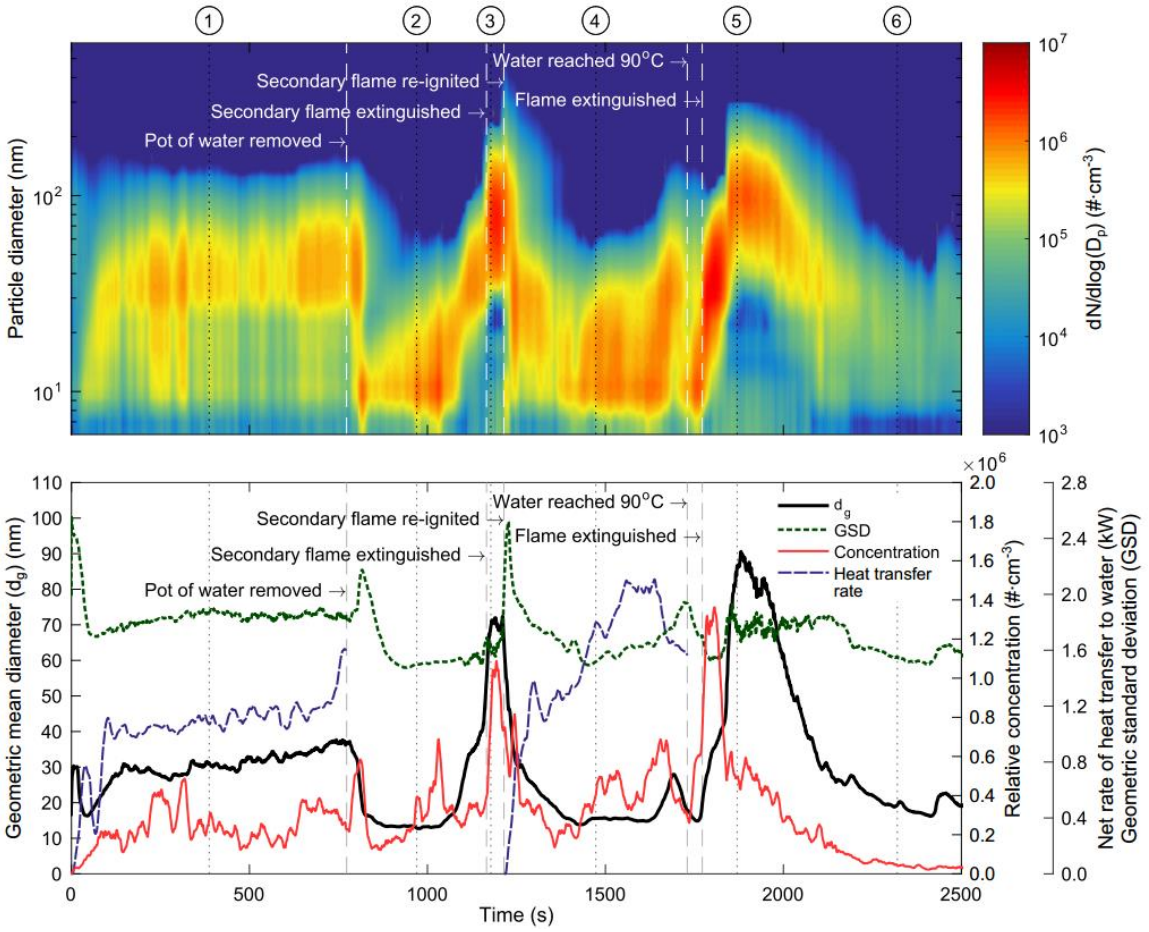

Figure 8. Top: Particle number size distribution. Bottom: Geometric mean diameter (d_g), geometric standard deviation (GSD), and relative concentration of PM emitted from the modular gasifier vs. time. Particle concentrations are post-dilution. The net rate of heat transfer to the water in the pot is also shown.[12]

During normal operation, the distribution was bimodal, with peaks at 10 nm and 40 nm, when a pot of water was on the stove (**Figure 8**). The geometric mean diameter (GMD) remained between 26 and 38 nm from 2 min after the stove was lit until the pot of water was removed. The relative mass emitted and relative mass emission rate were both 1.0.

When the pot of water was removed, the total particle number concentration remained similar, but the distribution became unimodal with a peak at 10 nm and the GMD decreased to approximately 15 nm. It is likely that removing the pot increased temperatures in the secondary combustion zone, increased the overall combustion efficiency, and enhanced the rate at which emitted particles were oxidized. As a result, the relative mass emission rate decreased to 0.63.

When the secondary flame extinguished, the particle number concentration increased sharply and the peak in concentration shifted to approximately 80 nm because volatiles released from the fuel bed were not being oxidized in the secondary combustion zone. The relative mass emission rate increased to 13 and the relative mass emitted was 3.7.

When the secondary flame was re-ignited and the pot was placed back on the stove, the particle number concentration decreased and size distribution became unimodal with a peak in number concentration at 10 nm. The relative mass emission rate decreased to 0.47 and the estimated relative mass emitted was 0.23. The variability in post-refueling emissions observed during previous tests made it difficult to draw conclusions about the factors that led to smaller particle emissions (relative to normal operation); however, the results indicated that emissions associated with refueling were dominated by transient increases that occurred when the secondary flame extinguished.

When the secondary flame extinguished again, the peak in number concentration increased to approximately 100 nm before decreasing to 20 nm during the char burn-out phase (**Figure 8**). The total particle number concentration also increased sharply and then decreased continuously during char burn-out. The decrease in particle size and number concentration most likely occurred because the rate of heat release from the fuel was decreasing and the volatile content of the fuel was being depleted. The relative mass emitted during shut-down was 7.5. Overall, the results demonstrated that changes in operational mode produced distinct changes in the size distribution and rate of particle emissions.

For more information, see the following documents:

- Tryner, J.; Tillotson, J. W.; Baumgardner, M. E.; Mohr, J. T.; DeFoort, M. W.; Marchese, A. J. The effects of air flow rates, secondary air inlet geometry, fuel type, and operating mode on the performance of gasifier cookstoves. *Environ. Sci. Technol.* **2016**, *50*, 9754–9763, DOI: 10.1016/10.1021/acs.est.6b00440.
- Tryner, J.; Volckens, J.; Marchese, A. J. Effects of operational mode on particle size and number emissions from a biomass gasifier cookstove. *Aerosol Sci. Technol.* **2018**, *52*(1), 87–97, DOI: 10.1080/02786826.2017.1380779.
- Tryner, J. Combustion Phenomena in Biomass Gasifier Cookstoves. Ph.D. Dissertation, Colorado State University, Fort Collins, CO, 2016. http://hdl.handle.net/10217/176745.

High-Speed Imaging of a 2-D Gasifier Cookstove Model

To gain a better understanding of the secondary combustion process, OH* chemiluminescence, acetone planar laser-induced fluorescence (PLIF), and OH PLIF images were collected from a burner designed to generate a two-dimensional replica of the secondary combustion zone in a gasifier cookstove. Chemiluminescence of electronically excited OH (OH*), which serves as a marker of heat release,[13] was imaged at 3 kHz to characterize the position and bulk dynamics of flame.[14,15] Acetone was used as a fuel tracer.[16,17] The gradient in OH concentration marks the high-temperature flame front, and regions of high OH concentration denote burned gases.[18] Acetone and OH PLIF images were collected at 10 kHz. The burner featured opposed planar air jets that formed an inverse non-premixed flame with the fuel in cross flow (**Figure 9**). The fuel was a mixture of CO, H_2, CH_4, C_2H_4, CO_2, N_2, and acetone that flowed up through a bed of glass beads. Images of five test cases were collected to investigate the influence of the fuel and air velocities on fuel-air mixing and flame dynamics: baseline, low air velocity, high air velocity, low fuel velocity, and high fuel velocity.

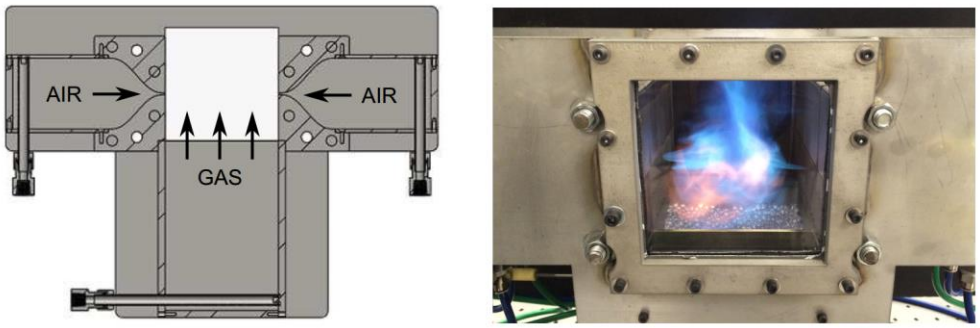

Figure 9. A cross-sectional diagram and photograph illustrating the operation of the 2-D burner. The burner was fueled with a gas mixture consisting of CO, H_2, CH_4, C_2H_4, CO_2, N_2 and acetone.[2]

OH* chemiluminescence images of the baseline and high air velocity cases revealed deflecting oscillation of the air jets. The jets started out parallel and opposed, but were then pushed apart in the vertical direction so that one jet moved on top of the other. Once the jets moved a certain distance apart, they swung back toward, and eventually past, each other, so that the jet that was on the top became the jet on the bottom and the jet that was on the bottom became the jet on the top.[19,20] This oscillation appeared to contribute to fuel/air mixing and subsequent heat release below the height of the air jets. In the other test cases (low fuel velocity, high fuel velocity, and low air velocity), oscillation was observed less frequently and may have been suppressed by convection in the vertical direction and/or buoyancy effects.

The acetone PLIF images revealed that higher air jet velocities resulted in more vigorous mixing of the air and fuel below the height of air injection (**Figure 10**). As a result, the reaction zone was located further below the top of the burner in comparison to the low air velocity case (see OH PLIF images in **Figure 11**). The average chemiluminescence images also indicated that heat release occurred further below the air jets (i.e., closer to the surface of the

fuel bed) as the velocity of the air jets increased. In accordance with these results, the lower emissions that were observed with higher secondary air jet velocities in the modular test bed may be attributable to better mixing of the air and fuel below the height of secondary air injection and a reaction zone that is located further below the top of the stove. The former would be expected to reduce the prevalence of fuel-rich zones that promote soot formation, and the latter would be expected to allow more time for oxidation of CO and PM before the hot gases in the secondary combustion zone impinge on the cold cooking surface.

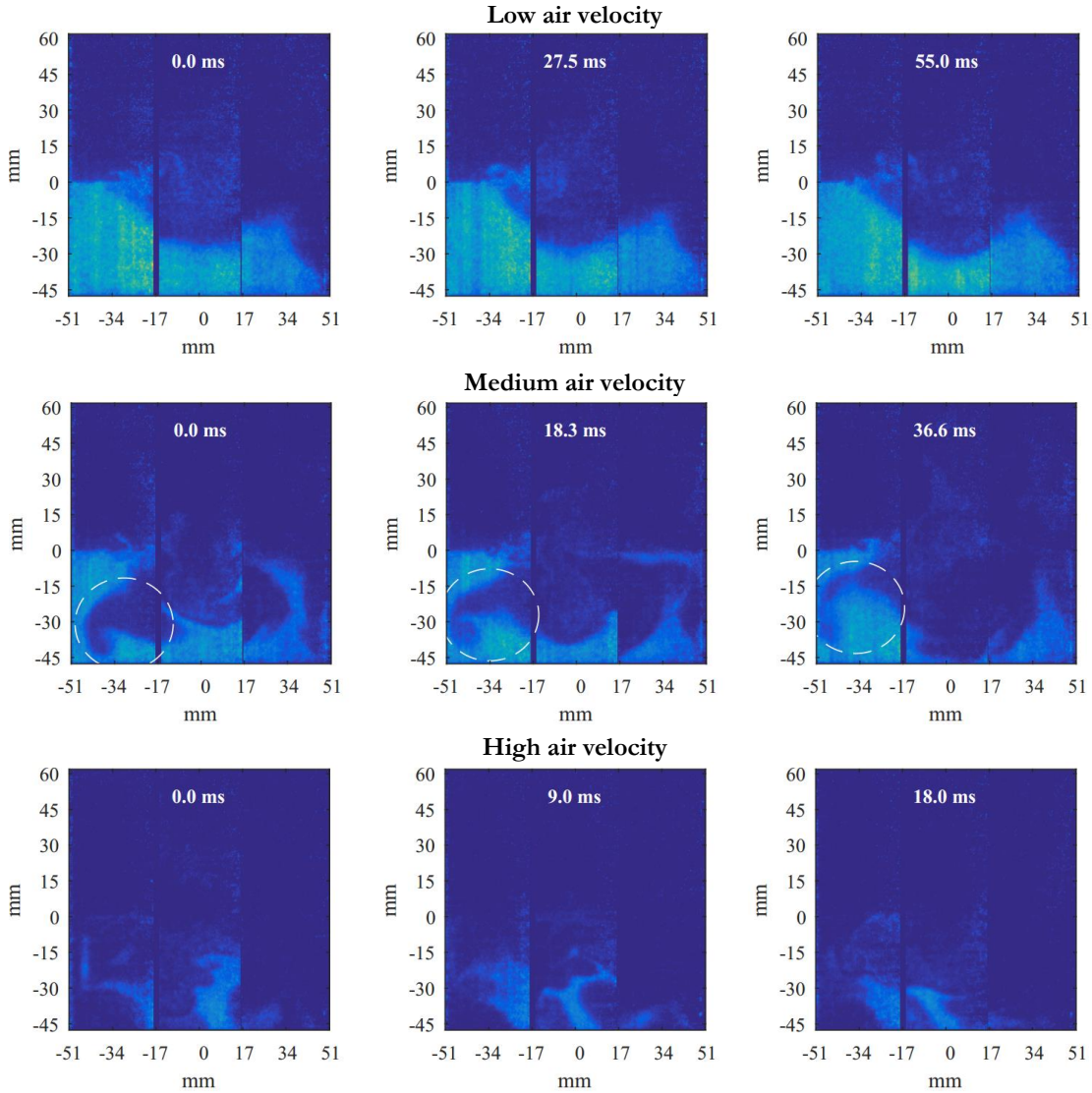

Figure 10. Sequences of acetone PLIF images from the low, medium, and high air velocity cases. The air jets are located at y = 0. The bright blue regions represent acetone fluorescence, which is a marker for unreacted fuel. In the medium air velocity images, a vortex that appears to be mixing the air and fuel is circled. Higher air jet velocities enhanced fuel-air mixing and resulted in the fuel being consumed further from the top of the stove (closer to the surface of the simulated fuel bed). [2]

The burner shown in **Figure 9** featured opposed planar jets, whereas the secondary combustion zone in biomass gasifier cookstoves typically features axisymmetric jets that may or may not impinge directly. Deflecting oscillation has been reported previously for

isothermal, non-reacting, unconfined opposed planar jets;[19–23] however, the literature suggests that deflecting oscillation does not occur for unconfined opposed axisymmetric jets.[24] As a result, there are limitations associated with use of planar jets as a model of the secondary combustion zone in a gasifier cookstove. The extent to which these limitations would affect the conclusions drawn above is unknown, since there are several differences between the burner examined here and isothermal, non-reacting, unconfined jets. Nonetheless, this system also serves as a useful validation case for the CFD model.

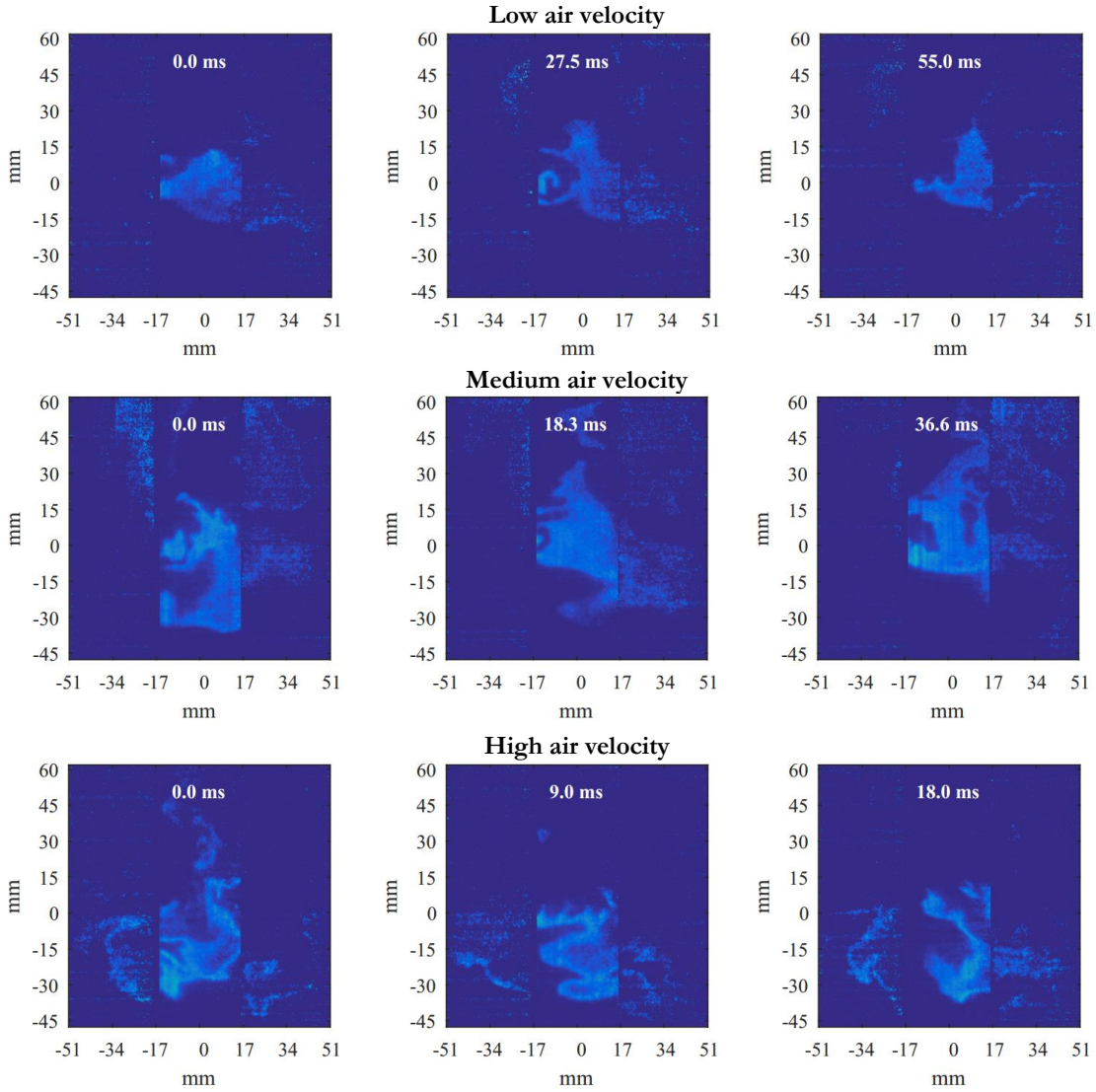

Figure 11. Sequences of OH PLIF images from the low, medium, and high air velocity cases. The air jets are located at y = 0. The bright blue regions represent OH fluorescence, which marks the high-temperature reaction zone and burnt gases. At higher air jet velocities, the reaction zone was further from the top of the stove.[2]

For more information, see the following documents:

- Tryner, J. Combustion Phenomena in Biomass Gasifier Cookstoves. Ph.D. Dissertation, Colorado State University, Fort Collins, CO, 2016. http://hdl.handle.net/10217/176745.

CFD MODELING

A CFD model called Chord was developed by the CFD & Propulsion group at Colorado State University to study the detailed mixing and combustion processes occurring in the secondary combustion zone of a gasifier cookstove.

Performance Criteria

Chord was designed to enable investigation of the effects of secondary air flow and variations in syngas composition on fluid and combustion physics, heat transfer in the gaseous phase, and flame stability in the secondary combustion zone. To achieve these goals, Chord features: (1) a finite-volume method compressible combustion code that is fourth-order accurate in time and space, (2) thermodynamic and transport properties modeled as functions of temperature, (3) curvilinear coordinate mapping for representation of complex geometries, (4) an Adaptive Mesh Refinement (AMR) scheme, (5) scalable performance across distributed memory, and (6) fine-grained parallelism and massive concurrency on a compute node. Chord was designed to be used with a reduced model of syngas (CO/H_2) combustion chemistry.

Model Description and Theory

Chord is a fourth-order finite-volume method algorithm for solving the fully coupled Navier-Stokes equations on structured grids. Chord is applied to simulate compressible, calorically or thermally perfect flows with species transport and chemical reactions. One main advantage of finite-volume methods is the inherent local conservation property. Additionally, finite-volume methods employed on Cartesian grids are computationally efficient and have well-understood characteristics in terms of solution accuracy. Traditionally, finite-volume methods have been constrained to second-order accuracy where the flux integrals are approximated using the midpoint rule. By increasing the order of accuracy of the algorithm from second- to fourth-order, we ensure that errors are reduced at twice the rate as the grid is uniformly refined and therefore improve the accuracy per unit memory. Consider an example in which, on a 3-D grid of $64\times64\times64$ (or $\approx2.6\times10^5$) cells, the norm of the solution error is 1×10^{-6}. To reduce this error by a factor of 16 using a fourth-order algorithm, we must refine the grid to $128\times128\times128$ ($\approx2.1\times10^6$) cells. To achieve the same error reduction with a second-order algorithm, we must refine the grid to $256\times256\times256$ ($\approx16.8\times10^6$) cells.

Modeling thermally perfect flows requires solving fitted polynomials to calculated thermodynamic and transport properties as functions of temperature. Although these polynomials can be computationally expensive, using lookup tables can reduce this cost. Additionally, nonlinear functions must be solved when converting conservative variables to primitive variables and resolving the reconstructed face values during the Riemann solution.

Brent's method combines aspects of the bisection method, secant method, and inverse quadratic interpolation to efficiently solve nonlinear problems.

Realistic geometries often do not allow the use of Cartesian meshes. To model flows in complex geometries, a structured curvilinear grid in physical space must be mapped to a Cartesian grid in computational space. This approach recovers Cartesian methods with some additional complexity associated with grid metrics. Using mapped grids has gained favor in the aerospace community, as wings are often easily meshed by this approach.

AMR allows the mesh resolution to be changed in response to the solution characteristics. Using AMR, large errors in specific regions can be resolved while avoiding the expense of increased resolution in regions with lower errors.[25] Care must be taken to ensure mapping and AMR are freestream preserving (i.e., that gradients are not introduced when flow is uniform).

Mathematics of the CFD Model

The Navier-Stokes equations, along with a set of species transport equations, can be transformed from physical space, $\vec{x}$, to computational space, $\vec{\xi}$, where $\vec{\xi}=\vec{\xi}(\vec{x})$, assuming the grid does not deform over time. The metric Jacobian (J) and transformation grid metrics (N^T) are defined by

$$J \equiv det\left(\vec{\nabla}_\xi \vec{x}\right) \tag{1}$$

$$N^T = J\vec{\nabla}_x \vec{\xi} \tag{2}$$

$$N = J\left(\vec{\nabla}_x \vec{\xi}\right)^T \tag{3}$$

where T denotes transpose operation. The divergence of a vector field in physical space is transformed to computational space using the mathematical relation shown in Equation 4.

$$\vec{\nabla}_x \cdot \vec{u} = \frac{1}{J}\vec{\nabla}_\xi \cdot (N^T \vec{u}) \tag{4}$$

The governing equations for a compressible gas on a mapped grid, transformed using grid metrics, are shown in Equations 5–8.

Continuity:
$$\frac{\partial}{\partial t}(J\rho) + \vec{\nabla}_\xi \cdot (N^T \rho \vec{u}) = 0 \tag{5}$$

Momentum:
$$\frac{\partial}{\partial t}(J\rho\vec{u}) + \vec{\nabla}_\xi \cdot \left(N^T\left(\rho\vec{u}\vec{u} + p\vec{\vec{I}}\right)\right) = \vec{\nabla}_\xi \cdot \left(N^T\vec{\vec{\mathcal{T}}}\right) + J\rho\vec{f} \tag{6}$$

Energy:
$$\frac{\partial}{\partial t}(J\rho e) + \vec{\nabla}_\xi \cdot \left(N^T\rho\vec{u}\left(e + \frac{p}{\rho}\right)\right) = \vec{\nabla}_\xi \cdot \left(N^T\left(\vec{\vec{\mathcal{T}}} \cdot \vec{u}\right)\right) - \vec{\nabla}_\xi \cdot \left(N^T\vec{\mathcal{Q}}\right) + J\rho\vec{f} \cdot \vec{u} \tag{7}$$

Species transport:
$$\frac{\partial}{\partial t}(J\rho c_n) + \vec{\nabla}_\xi \cdot (N^T \rho c_n \vec{u}) = -\vec{\nabla}_\xi \cdot \left(N^T\vec{\mathcal{J}}_n\right) + J\rho\dot{\omega}_n, \quad n = 1 \ldots N_s \tag{8}$$

where c_n is the mass fraction of the n^{th} species and N_s is the total number of species. The identity tensor is denoted $\vec{\vec{I}}$ and the total specific energy is $e = |\vec{u}|^2/2 + \sum_1^{N_s} c_n h_n - p/\rho$. Body force terms are specified as $\vec{f}$.

Pressure is determined by the ideal gas law (assuming the flow is thermally perfect ideal gas):

$$p = \sum_{n=1}^{N_s} \rho c_n R_n T \tag{9}$$

The stress tensor and the molecular heat flux vector on the mapped grids are represented by $\vec{\vec{\mathcal{T}}}$ and $\vec{\mathcal{Q}}$. The mapped stress tensor is defined by Equation 10.

$$\vec{\vec{\mathcal{T}}} = 2\mu\left(\vec{\vec{S}} - \frac{1}{3}J^{-1}\vec{\vec{I}}\vec{\nabla}_\xi \cdot (N^T\vec{u})\right) \tag{10}$$

The molecular heat flux is modeled using Fourier's law (Equation 11) and mass diffusion is modeled using Fick's law (Equation 12).

$$\vec{\mathcal{Q}} = -\left(\kappa\frac{N}{J}\vec{\nabla}_\xi T - \sum_{n=1}^{N_s} h_n\vec{\mathcal{J}}_n\right) \tag{11}$$

$$\vec{\mathcal{J}}_n = -\rho D_n\frac{N}{J}\vec{\nabla}_\xi c_n - \frac{D_{T,n}}{T}\frac{N}{J}\vec{\nabla}_\xi T \tag{12}$$

Mass diffusion can occur in the presence of temperature gradients (called the Soret effect), large pressure gradients, or body forces like electromagnetic forces. Additionally, temperature gradients can form in the presence of concentration gradients (the Dufour effect). These effects are generally small and can be neglected. Currently, we assume that the thermal (Soret) diffusion coefficient ($D_{T,n}$) is equal to zero for all species. Therefore, mass diffusion is assumed to occur only as a result of concentration gradients, as shown in Equation 13.

$$\vec{\mathcal{J}}_n = -\rho D_n\frac{N}{J}\vec{\nabla}_\xi c_n \tag{13}$$

Thermodynamic and transport properties must be approximated to close the system of governing equations. For each species, the specific heat at constant pressure is defined by:[26]

$$\frac{c_{p,n}}{R_n} = \frac{a_{1,n}}{T^2} + \frac{a_{2,n}}{T} + a_{3,n} + a_{4,n}T + a_{5,n}T^2 + a_{6,n}T^3 + a_{7,n}T^4 \tag{14}$$

and the specific heat at constant pressure of the mixture is $c_p = \sum_{n=1}^{N_s} c_n c_{p,n}$. Similarly, the total specific enthalpy is defined by:

$$\frac{h_n(T;T^0)}{R_n T} = \frac{H_n}{R_u T} = -\frac{a_{1,n}}{T^2} + \frac{a_{2,n}}{T}\ln T + a_{3,n} + a_{4,n}\frac{T}{2} + a_{5,n}\frac{T^2}{3} + a_{6,n}\frac{T^3}{4} + a_{7,n}\frac{T^4}{5} + \frac{a_{8,n}}{T} \tag{15}$$

where $a_{8,n}$ is the integration constant for enthalpy. The total specific enthalpy of the mixture is $h = \sum_{n=1}^{N_s} c_n h_n$. The specific enthalpy is the sum of the sensible enthalpy, $h_n^s(T;T^0)$, and the heat of formation, $\Delta_f h_n(T^0)$, relative to a reference temperature, T^0. The total specific enthalpy values provided by Gordon and McBride use T^0 = 298.15 K. Therefore, the polynomial in Equation 15 is equal to the sensible energy plus the heat of formation at 298.15 K:

$$h_n(T; 298.15\ K) \equiv \Delta_f h_n(298.15\ K) + h_n^s(T; 298.15\ K) \tag{16}$$

Currently, the reference temperature in the model is 0 K, meaning we define an additional enthalpy constant for each species, h_n^c, that adds in the difference in the heat of formation and sensible enthalpy from 0 to 298.15 K:

$$h_n^c \equiv \Delta_f h_n(0\ K) - \Delta_f h_n(298.15\ K) + h_n^s(298.15\ K; 0\ K) - h_n^s(0\ K; 0\ K) \tag{17}$$

The constant in Equation 17 is added to Equation 15 to define the total specific enthalpy as:

$$h_n \equiv h_n(T; 0\ K) = h_n(T; 298.15\ K) + h_n^c \tag{18}$$

The specific molar entropy can be solved using the fitted polynomial shown in Equation 19, where $a_{9,n}$ is the integration constant for entropy.

$$\frac{S_n}{R_u} = -\frac{a_{1,n}}{2T^2} + \frac{a_{2,n}}{T} + a_{3,n}\ln T + a_{4,n}T + a_{5,n}\frac{T^2}{2} + a_{6,n}\frac{T^3}{3} + a_{7,n}\frac{T^4}{4} + a_{9,n} \tag{19}$$

The values for dynamic viscosity (μ) and thermal conductivity (κ) are calculated using a curve fit polynomial.[26] The coefficients were fitted using the following forms:

$$\ln \mu_n = b_{1,n}\ln T + \frac{b_{2,n}}{T} + \frac{b_{3,n}}{T^2} + b_{4,n} \tag{20}$$

$$\ln \kappa_n = c_{1,n}\ln T + \frac{c_{2,n}}{T} + \frac{c_{3,n}}{T^2} + c_{4,n} \tag{21}$$

where $b_{1-4,n}$ and $c_{1-4,n}$ represent the coefficient for the n^{th} species μ and κ, respectively. The coefficients are provided by McBride et al.[27] The mixture values of μ and κ are calculated using the mixture-based formulas shown in Equation 22–23, where the mole fractions (χ_n) are defined as shown in Equation 24.[28]

$$\mu = \frac{1}{2}\left[\sum_{n=1}^{N_s}\mu_n\chi_n + \left(\sum_{n=1}^{N_s}\frac{\chi_n}{\mu_n}\right)^{-1}\right] \tag{22}$$

$$\kappa = \frac{1}{2}\left[\sum_{n=1}^{N_s}\kappa_n\chi_n + \left(\sum_{n=1}^{N_s}\frac{\chi_n}{\kappa_n}\right)^{-1}\right] \tag{23}$$

$$\chi_n = \frac{c_n}{M_n\sum_{j=1}^{N_s}\frac{c_j}{M_j}} \tag{24}$$

The coefficients in Equations 14–15 and 19–21 actually represent two sets of coefficients for $200 \leq T < 1000$ K and $1000 \leq T < 6000$ K. The mixing rule for μ and κ are less accurate than semi-empirical methods and methods that account for binary interactions between species. For example, the mixture-based approach produced an error of 5.4% for the chemicals tested by Mathur et al.[28]. However, the semi-empirical approach can increase the computational cost of the transport properties by 3× compared to the mixture-based approach.

The mass diffusion coefficient (D_n) can be obtained from a given Schmidt number (Sc) using Equation 25 or from a given Lewis number (Le) using Equation 26.

$$D_n = \frac{\mu}{\rho Sc} \tag{25}$$

$$D_n = \frac{\kappa}{\rho c_p Le} \tag{26}$$

The current assumption that the mass diffusion coefficient is based on a constant Schmidt or Lewis number and is the same for all species neglects the statistical aspects of particle collisions. This assumption is admittedly problematic when the molecular weights and structures vary significantly between different species.

Chemical reactions are modeled using finite-rate chemistry. The general form of the law of mass action[29] is used to calculate the mean reaction rate for the n^{th} species:

$$\dot{\omega}_n = \frac{M_n}{\rho}\sum_{r=1}^{N_r}\left(\nu''_{n,r} - \nu'_{n,r}\right)\left(k_{f,r}\prod_{j=1}^{N_s}[X_j]^{\nu'_{j,r}} - k_{b,r}\prod_{j=1}^{N_s}[X_j]^{\nu''_{j,r}}\right) \tag{27}$$

The Arrhenius approach is used to calculate the forward reaction rate:

$$k_{f,r} = A_r T^{\beta r}\exp\left(\frac{-E_{a,r}}{R_c T}\right) \tag{28}$$

The molar concentration of the n^{th} species is defined by:

$$[X_n] = \frac{\rho c_n}{M_n} \tag{29}$$

For reversible reactions, the backward reaction rate is defined by:

$$k_{b,r} = \frac{k_{f,r}}{K_{eq,r}} \tag{30}$$

$$K_{eq,r} = exp\left(\sum_{n=1}^{N_s}\nu_{n,r}\frac{-G_n}{R_u T}\right)\left(\frac{p_{atm}}{R_u T}\right)^{\sum_{n=1}^{N_s}\nu_{n,r}} \tag{31}$$

Additionally, $\nu_{n,r} = \nu''_{n,r} - \nu'_{n,r}$ and G_n is the Gibb's free energy, defined by:

$$\frac{G_n}{R_u T} = \frac{H_n}{R_u T} - T\frac{S_n}{R_u} \tag{32}$$

Some reactions are three-body reactions, which require a third body, denoted M, to stabilize the reaction. If three-body reactions are present, Equation 27 becomes:

$$\dot{\omega}_n = \frac{M_n}{\rho}\sum_{r=1}^{N_r}\left(\nu''_{n,r} - \nu'_{n,r}\right)\left(\sum_{i=1}^{N_s}\alpha_{i,r}[X_i]\right)\left(k_{f,r}\prod_{j=1}^{N_s}[X_j]^{\nu'_{j,r}} - k_{b,r}\prod_{j=1}^{N_s}[X_j]^{\nu''_{j,r}}\right) \tag{33}$$

Where $\alpha_{i,r} = 1$ for all species unless specified otherwise in the reaction mechanism.

Model Verification and Validation

The algorithm was verified to be fourth-order accurate using a two-dimensional vortex convection and diffusion problem similar to the one described by Yee et al.[30] This problem was selected due to the absence of shock waves and turbulence. The flow was initialized as a uniform mixture of 23.3% O_2 and 76.7% H_2 by mass.

The vortex radius (r_c), a vortex center (x_c, y_c), a vortex strength (Γ), a stagnation temperature (T_∞), and a stagnation pressure (p_∞) were all specified. The gas constant (R_∞) was set based on the uniform initial mixture mass fractions. The radius was given by Equation 34.

$$r = \sqrt{\bar{x}^2 + \bar{y}^2} \tag{34}$$

$$(\bar{x}^2 + \bar{y}^2) = (x - x_c, y - y_c) \tag{35}$$

The initial velocity is perturbed using:

$$(u, v) = (u_\infty - \bar{y}v_\theta, v_\infty - \bar{x}v_\theta) \tag{36}$$

$$v_\theta = \frac{\Gamma}{2\pi}\exp\left(\frac{1 - r^2}{2}\right) \tag{37}$$

The pressure is initialized as shown in Equation 38.

$$p = p_\infty\left(1 - \left(\frac{\Gamma}{2\pi}\right)^2\left(\frac{\exp(1 - r^2)}{2T_\infty R_\infty}\right)\right) \tag{38}$$

The initial temperature was solved using the isentropic relation shown in Equation 39 assuming a constant γ.

$$T = T_\infty\left(\frac{p}{p_\infty}\right)^{\frac{\gamma-1}{\gamma}} \tag{39}$$

The density was initialized using the ideal gas law, as shown in Equation 40.

$$\rho = \frac{p}{TR_\infty} \tag{40}$$

Accuracy was verified using a case with T_∞ = 2900 K, p_∞ = 101325 Pa, and Γ = 20 $m^2 \cdot s^{-1}$. These values were chosen to minimize the Reynolds number while maintaining a perturbation in pressure, density, and temperature. The Reynolds number was minimized to ensure that the flow remained laminar and increase the influence of the diffusive fluxes on the solution. The vortex was stationary, meaning $u_\infty = v_\infty = 0$ $m \cdot s^{-1}$. The dynamic viscosity and thermal conductivity were $\mu = 4.515 \times 10^{-5}$ Pa·s and $\kappa = 1.084$ $W \cdot m^{-1}K^{-1}$. The Reynolds number, Mach number, and Prandtl number were evaluated for this test case as shown in Equations 41–43.

Reynolds number:
$$Re = \frac{\rho\Gamma}{\mu} = 4800 \tag{41}$$

Mach number: $$Ma = \frac{|u|_{max}}{a} = \frac{\Gamma/(2\pi)}{\sqrt{\gamma R T_\infty}} = 9.16 \times 10^{-4} \quad (42)$$

Prandtl number: $$\mathrm{Pr} = \frac{\mu c_p}{\kappa} = 0.596 \quad (43)$$

The computational domain was a 30 m × 30 m square and periodic boundary conditions were enforced at both extents. The vortex center was at the middle of the domain (x_c, y_c) = (15, 15). Numerical solution errors were measured with the L_∞-, L_1-, and L_2-norms at t = 0.084488 s. The convergence rates between consecutive grid resolutions were computed using Richardson extrapolation.[31] The pre-coarse, coarse, medium, and fine meshes were 128×128, 256×256, 512×512, and 1024×1024, respectively. The post-fine solution on a 2048×2048 mesh was used as a "true" solution for computing error norms during the Richardson extrapolation procedure. The time step for the coarse grid (2.1122×10^{-5} s) was reduced proportionally as the grids were refined (1.0561×10^{-5} s for medium, etc.). The solution was run to time t_f = 0.084488 s. The error norms and the corresponding rates at which error was reduced for conservative solution variables (density, momentum, energy) as the grid was refined are listed in **Table 1**. The convergence rates for the solution variables approached 4, indicating that the algorithm is fourth-order accurate. The slopes of the solution error norms in **Figure 12** demonstrate fourth-order convergence for the x-momentum.

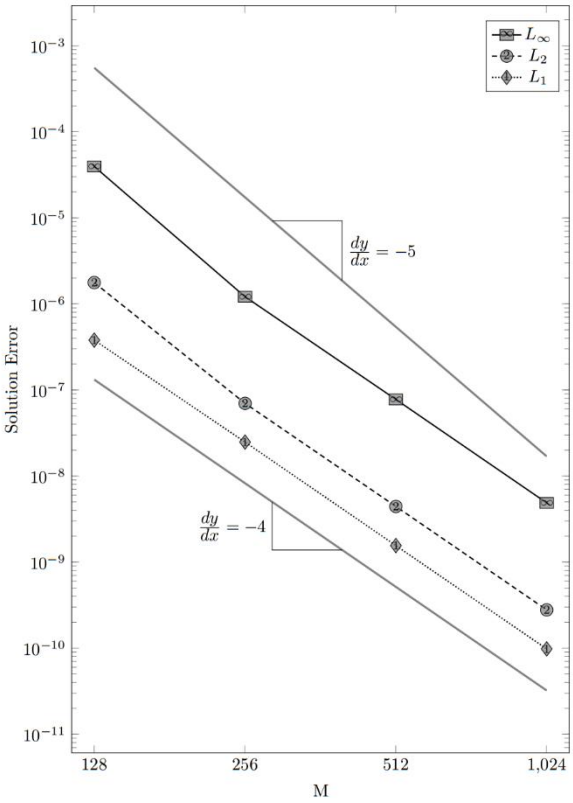

Figure 12. Solution error of ρu versus grid size at 0.084488 s for the vortex.

Table 1. Stationary vortex solution errors measured with the measured with the L_∞-, L_1-, and L_2-norms at t = 0.084488 s and convergence rates between consecutive grid resolutions.

Variable	L norm	128×128	Rate	256×256	Rate	512×512	Rate	1024×1024
ρ	L_∞	1.791e-10	2.897	2.405e-11	4.137	1.367e-12	3.987	8.616e-14
	L_1	4.061e-11	2.748	6.047e-12	3.958	3.891e-13	3.988	2.453e-14
	L_2	5.350e-11	2.782	7.780e-12	3.976	4.944e-13	3.989	3.114e-14
ρu	L_∞	3.952e-05	5.028	1.212e-06	3.965	7.758e-08	3.994	4.871e-09
	L_1	3.793e-07	3.935	2.480e-08	3.996	1.555e-09	3.989	2.789e-11
	L_2	1.769e-06	4.662	6.987e-08	3.979	4.432e-09	3.994	2.781e-10
ρe	L_∞	6.507e-03	2.897	8.735e-04	4.137	4.963e-05	3.987	3.130e-06
	L_1	1.475e-03	2.747	2.196e-04	3.958	1.413e-05	3.988	8.911e-07
	L_2	1.943e-03	2.782	2.826e-04	3.976	1.796e-05	3.989	1.131e-06

The ability to model reacting flows using Chord was validated using a 1-D problem involving advection of a plateau of H_2 through a domain of higher temperature O_2. The species mass fractions were initialized as shown in Equations 44 and 45.

$$c_{H_2} = \frac{1}{2}\left[1 + \tanh\left(C_1\left[\frac{L_p}{2} - |x - x_0|\right]\right)\right] \tag{44}$$

$$c_{O_2} = 1 - c_{H_2} \tag{45}$$

where C_1 determines the sharpness of the front (set to 80 cm^{-1} in this case), x_0 is the location of the center of the H_2 plateau (3.7 cm), and L_p is the width of the plateau (0.6 cm).

Density was initialized as shown in Equation 46, where T_{H_2} = 1000 K and T_{O_2} = 2000 K. The entire domain was initialized to p_{atm}.

$$\rho = \left(\frac{c_{H_2} R_{H_2} T_{H_2} + c_{O_2} R_{O_2} T_{O_2}}{p_{atm}}\right)^{-1} \tag{46}$$

The simulation used AMR; the base grid had a spacing of Δx = 0.02 cm with three refined levels, all with refinement ratios of 2 (Δx = 0.01, 0.005, 0.0025 cm).

The numerical solution from Chord was compared to the solution from Attal et al.[32] Species mass fractions and temperature profiles at t = 100 μs are shown in **Figure 13**. The profiles and interface locations predicted by Chord agreed with the prior results. Chord predicted a greater amount of O_2 and H_2O near the leading and trailing fronts and less H_2 at the edges of the central plateau. These discrepancies could be due to the different methods used to model transport properties. Attal et al.[32] computed dynamic viscosity using a semi-empirical formula,[33] whereas Chord uses a mixture-based formula (Equation 22). Chord predicted a lower maximum temperature at the leading and trailing fronts and a greater length between the temperature peaks. The Attal et al.[32] solution undershot the temperature at the leading and trailing fronts. We believe Chord predicted the temperature profile more accurately due to the higher order accuracy of the algorithm.

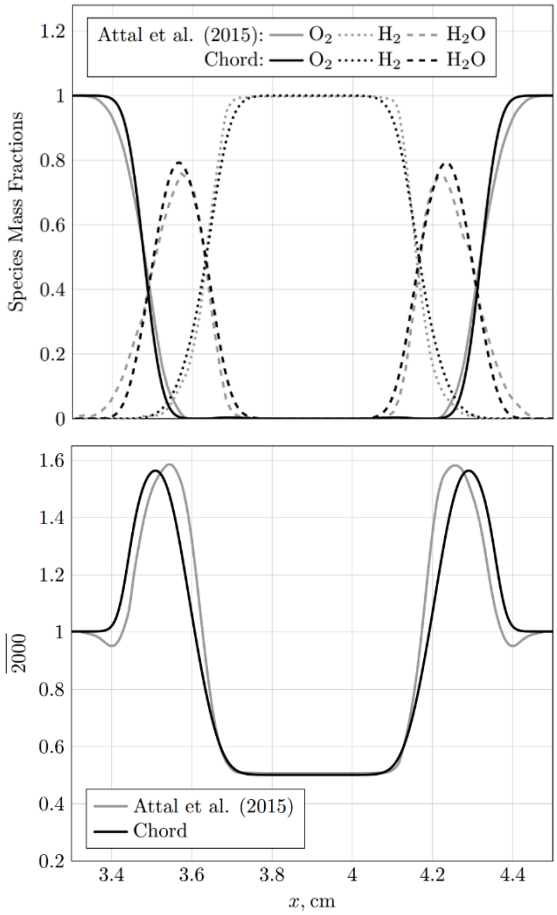

Figure 13. Mass fraction (top) and temperature (bottom) profiles for the reacting flame front problem at t = 100 μs.

Modeling of the 2-D Burner used for Chemiluminescence and PLIF Imaging

The computational domain used to model the two-dimensional burner (**Figure 9**) is shown in **Figure 14**. In the model, a fuel-air mixture flowed in the positive y-direction between two vertical walls, while air was injected horizontally from two jets located on the vertical walls. The height and width of the burner (L_y and L_x) were 0.1016 m. The distance from the top of bed of glass beads (which was modeled as the burner inlet) to the bottom of the jets (L_w) was 0.0492 m. The height of the jets (L_j) was 1.6×10^{-3} m. The computational domain had dimensions of $L_x \times 8L_y$ to set the outlet boundary far from the top of the burner and minimize interference on the outflow from the interior flow.

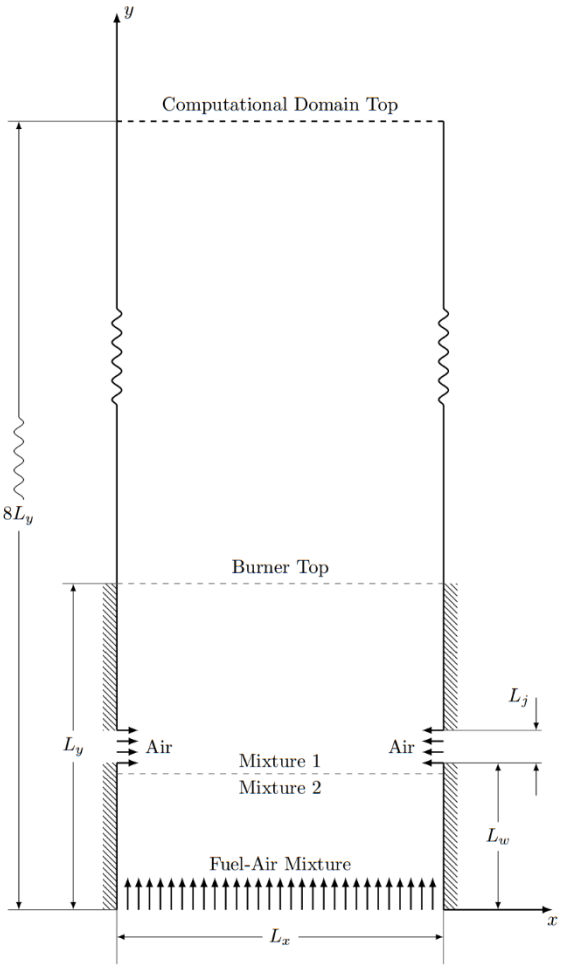

Figure 14. The burner and computational domain geometry.

A fuel-air mixture (5.51% CH_4, 22.02% O_2, and 74.47% N_2 by mass fraction) flowed into the domain from the lower y boundary with a y-velocity of 0.075 m·s^{-1} at a temperature of 313 K. At this boundary, the pressure was extrapolated from the interior of the domain. The air jets (23.30% O_2 and 76.70% N_2 by mass fraction) were injected horizontally into the domain with velocities of 4.96 m·s^{-1} at a temperature of 293 K. At the jet boundaries, pressure was again extrapolated from the interior. The walls were no-slip for $y < L_y$ but slip for $y \geq L_y$. The outlet used a zero gradient Neumann condition for all variables.

The initial mixture in the domain was quiescent. At $y \geq 0.04$ m ("Mixture 1" in **Figure 14**) the initial fluid consisted of 15.14% CO_2, 12.39% H_2O and 72.46% N_2 at T=298 K. The remainder of the initial fluid ("Mixture 2" in **Figure 14**) had the same composition and temperature as the air from the jets. "Mixture 1" and "Mixture 2" were both set to atmospheric pressure.

The base grid was 32×256 with 2 additional refinement levels. The first level was refined 2 times and the second level was refined 4 times. Cells were dynamically tagged for refinement based on a gradient of density. The time-step, dynamic viscosity, thermal conductivity, and diffusion coefficient were calculated using the methods outlined above. Subcycling was used

during the solution. The solution was run for one convective time scale (i.e., the time required for the inflow to reach the top of the burner; approx. 1.345 s.). The mesh was adapted based on the physics criteria such as vorticity and species gradients.

The O2 mass fraction within the computational domain is shown at three time steps (t = 0.002 s, t = 0.101 s, and t = 1.652 s) in **Figure 15**. The fluid structures produced by the jets and the fluid interactions between the bottom inlet flow and initial flow field can be seen. At t = 0.02 s, the fluid jets were symmetric. At t = 0.101 s, the symmetry began to break down as the two jets interacted with each other. Much later in the solution (t = 1.652 s) there was no symmetry. The jets appeared to overlap one another and the O_2 began to mix more uniformly throughout the domain. This asymmetric process was also observed in the OH* chemiluminescence images from the two-dimensional burner.

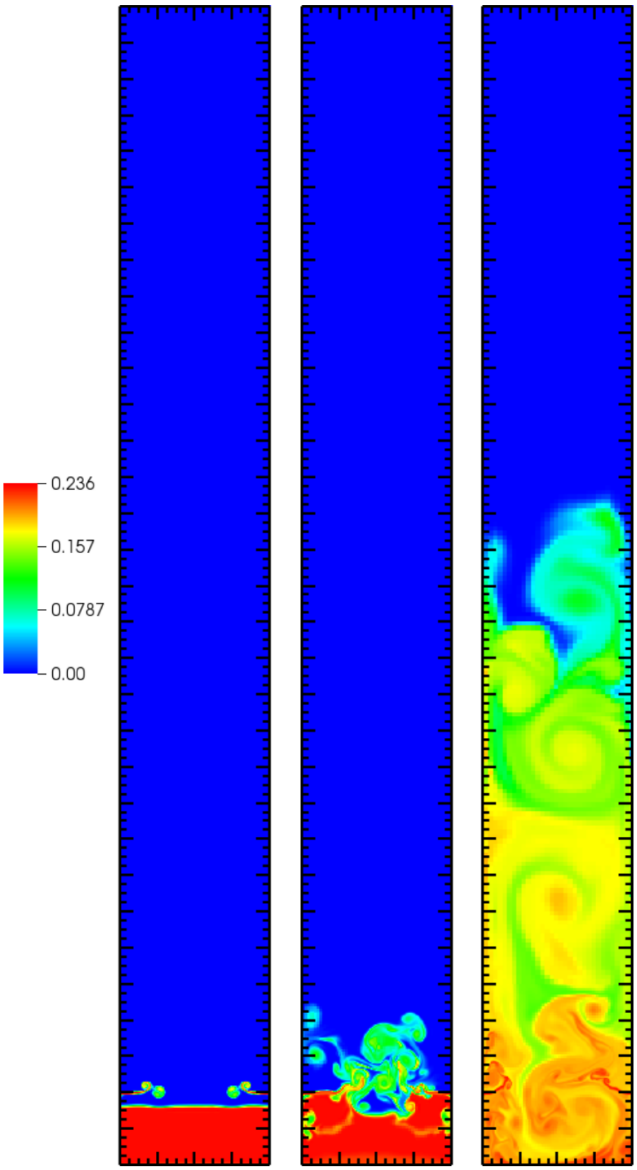

Figure 15. The mass fraction of O_2 in the computational domain at t = 0.02 s (left), t = 0.101 s (center), and t = 1.652 s (right) during a simulation of the two-dimensional burner geometry.

Hardware Requirements

Chord is highly parallelized and is designed to run on today's high-performance computing (HPC) architectures. The CFD & Propulsion group maintains 11 Linux workstations and a high-performance compute server. Researchers have access to three tiers of computing power.

Tier 1 consists of the individual workstations. The workstations are built to high-end consumer-grade specifications and feature parallel technologies that will be encountered on supercomputers including AVX registers and GPU computing. The workstations support development, pre- and post-processing, and limited performance testing and engineering simulations.

Tier 2 is the internal high performance compute server. The server consists of nine compute nodes and 24 TB of storage connected by a 40 Gbps Infiniband network. Four of the compute nodes each contain 20 Intel Sandy Bridge CPU cores, an Nvidia Tesla K20 GPU, and a 128 GB of memory. Five of the compute nodes are each configured with 24 Intel Haswell cores and 64 GB of memory. In total, there are 200 cores on the compute nodes. The server supports GPU-Direct RDMA so that MPI can be used to communicate between CPUs and GPUs. The workstations and internal server are connected by an island 10 Gbps network.

Tier 3 consists of external supercomputers such as the ISTeC Cray at CSU. These servers present separate working environments and are accessed for large scale performance testing and large production simulations.

For more information on the CFD model, see the following documents:

- Guzik, S. M.; Gao, X.; Owen, L. D.; McCorquodale, P.; Colella, P. A Freestream-Preserving Fourth-Order Finite-Volume Method in Mapped Coordinates with Adaptive-Mesh Refinement. *Comput. Fluids* **2015**, *123*, 202–217. DOI: 10.1016/j.compfluid.2015.10.001.
- Owen, L. D.; Guzik, S. M.; Gao, X. High-Order CFD Modeling of Multispecies Flows. Presented at the Western States Section of the Combustion Institute – 2015 Fall Technical Meeting, Provo, UT, October 5–6, 2015; 134IE-0030.
- Gao, X.; Owen, L. D.; Guzik, S. M. J. A Parallel Adaptive Numerical Method with Generalized Curvilinear Coordinate Transformation for Compressible Navier-Stokes Equations. *Int. J. Numer. Methods Fluids* **2016**, *82* (10), 664–688. DOI: 10.1002/fld.4235.
- Owen, L. D.; Guzik, S. M.; Gao, X. A Fourth-Order Viscous Operator on Mapped Grids. Presented at the 54th AIAA Aerospace Sciences Meeting, AIAA SciTech Forum, San Diego, CA, January 4–8, 2016; AIAA 2016-0604. DOI: 10.2514/6.2016-0604.
- Owen, L. D.; Guzik, S.; Gao, X. A Fourth-Order Finite-Volume Algorithm for Compressible Flow with Chemical Reactions on Mapped Grids. Presented at the 23rd AIAA Computational Fluid Dynamics Conference, AIAA AVIATION Forum, Denver, CO, June 5–9, 2017; AIAA 2017-4498. DOI: 10.2514/6.2017-4498.
- Owen, L. D.; Guzik, S. M.; Overton, N.; Gao, X. A High-Order Adaptive Algorithm for Multispecies Gaseous Flows on Mapped Domains. *J. Comput. Fluids* **2017**, Submitted.

All artifacts of this research are placed under a Mercurial version control system. The Mercurial repository is maintained at CSU for primary development (http://cfd-repo.engr.colostate.edu/).

Development of a Reduced Chemical Kinetic Model for CFD Modeling

A computationally efficient gas phase combustion chemistry model was developed for use with the CFD model of the secondary combustion zone. This model describes the combustion of H_2 and H_2/CO blends (syngas), with or without significant addition of N_2, H_2O, and CO_2 in the unburned gas mixture. Variants of this model may also serve as hierarchical cores upon which models for other fuels/fuel components (such as CH_4) can be built. Rate coefficients,[34–41] thermochemistry,[42–44] and transport properties[34,40,45,46] based on recent theory and/or experiment were assembled to form the base syngas combustion model. This base model was validated against literature ignition delay time, laminar burning rate, and flow reactor species-time history profiles at pressures relevant to cookstove applications ($0.5 \leq P \leq 2.0$ atm) and a broad range of characteristic temperatures, equivalence ratios, and unreacted mixture compositions. The 14 species, 43 effective reaction base model was subsequently reduced to an 11 species, 21 effective reaction final model.

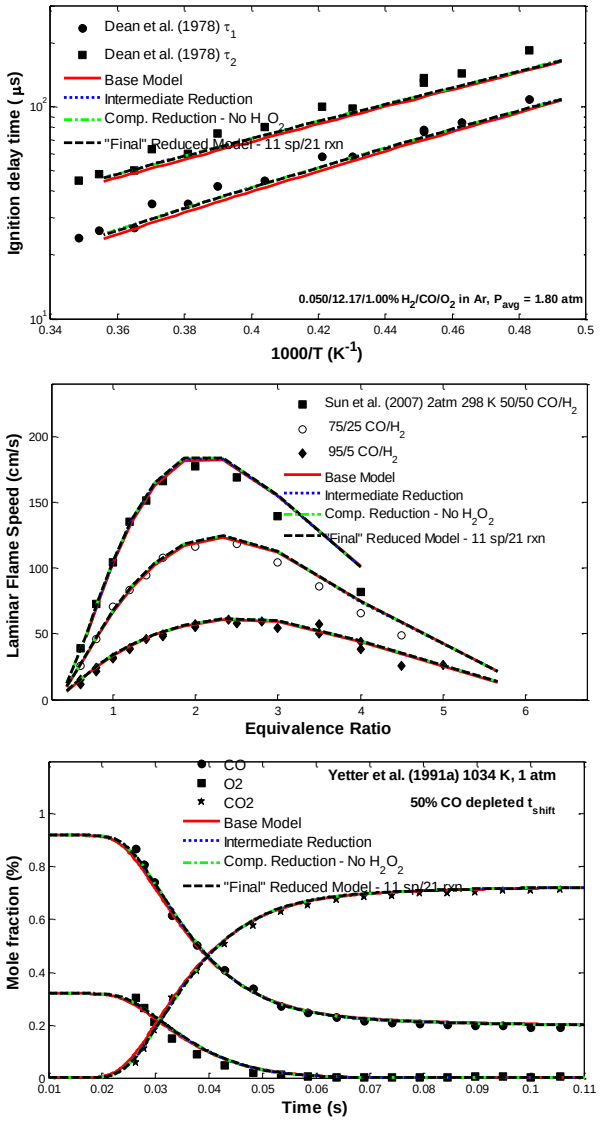

Figure 16. Gas phase kinetic model prediction exemplars of experimental ignition delay time[48] (top), laminar burning velocity[49] (middle), and chemical species evolution profile[50] (bottom) measurements. Predictions of several model variants are shown.

Though the reduction essentially halved the number of reactions considered, it resulted in negligible differences between predictions of the base and final models at each validation condition (**Figure 16**). Rough computational time scaled of t ~ N3 (corresponding to Jacobian matrix inversion for implicit numerical schemes, and where N is the number of kinetic model chemical species) results in an acceleration factor of ~2 for the 11 species reduced model relative to the 14 species base model. Further reduction would significantly impair the predictive capability of the model. CHEMKIN-compatible (e.g., Kee et al.[47]) variants of the model can be provided upon request.

PROTOTYPE DEVELOPMENT AND TESTING

The knowledge gained from testing the modular gasifier was used to develop a prototype TLUD gasifier cookstove. The first prototype (P1; **Figure 17**) was designed with the goal of replicating the performance of the lowest-emitting modular gasifier configurations in a small, standalone, fan-powered stove. The combustion chamber featured 9 2-mm-diameter primary air inlet holes near the base, 6 2-mm-diameter early secondary air injection holes part-way up the side, and 32 2-mm-diameter secondary air inlet holes near the top.

Figure 17. The P1 prototype was a standalone fan-powered unit. It was used to develop pressure curves that relate flow rate to fan speed.

Unlike the modular test bed, the P1 prototype did not feature independent control over the primary and secondary air flow rates. Instead, air flowed through a common pressurized plenum—formed by the annulus between the concentric cylinders of the combustion chamber and the outer shell of the stove—before entering the combustion chamber through the primary and secondary air inlet holes. The primary and secondary air flow rates were functions of plenum pressure, gas density, and the areas of the primary and secondary air inlets. Initially, the P1 prototype was tested with compressed air. Air was metered into the plenum using a mass flow controller, and the pressure inside the plenum was mapped to the total mass flow of air (primary + secondary) over a range of flow rates.

In the next iteration of the P1 prototype, airflow was provided by a fan. A microcontroller was used to control the fan speed using pulse width modulation (PWM). Use of PWM allowed for precise, repeatable control of fan speed under a range of operating conditions. The fan speeds were adjusted to match the plenum pressures associated with the desired mass flow rates (as determined from initial testing with compressed air).

The second prototype (P2; **Figure 18**) was a field-ready unit that would be suitable for pilot testing to obtain feedback from users. The size and appearance of the P2 was based on prior market studies conducted by Envirofit International. To achieve the proper ratio of secondary to primary air flow, the combustion chamber featured 7 2-mm-dia. primary air inlet holes near the base, 6 2-mm-dia. early secondary air injection holes part-way up the side, as well as 24 4-mm-dia. and 8 2-mm-dia. secondary air inlet holes near the top. To reduce the gasification rate during the simmer phase of cooking and make the P2 suitable for low-power operation, the diameter of the bottom half of the combustion chamber was reduced to 75 mm. Like the P1, the P2 plenum pressure was mapped to known mass flow rates using compressed air and then to fan speeds set using PWM.

The P2 prototype underwent laboratory testing at CSU and Lawrence Berkeley National Laboratory (LBNL) to characterize high-power emissions, low-power emissions, and fuel efficiency. High-power performance was evaluated by boiling 5 L of water using a stove that started out cold. Low-power performance was evaluated by simmering the water for 15 minutes immediately after it boiled. Test results from CSU for the stove fueled with two different initial masses of Lodgepole Pine wood pellets (600 g and 550 g) are shown in **Table 2**. Because the diameter of the top portion of the fuel chamber (109 mm) is larger than the diameter of the bottom portion (75 mm), the stove operates at a higher power for a longer period of time when fueled with a larger mass of pellets. As a result, when the stove if fueled with 600 g of pellets, the time to boil is shorter (27 minutes vs. 33 minutes) and $PM_{2.5}$ emissions are higher. The Tier 4 targets for high-power $PM_{2.5}$ emissions and indoor $PM_{2.5}$ emissions were not met when the stove was fueled with 600 g of pellets, but were met when the stove was fueled with 550 g of pellets. The Tier 4 targets for high-power CO emissions; low-power specific fuel consumption, CO emissions, and $PM_{2.5}$ emissions; as well as and indoor CO emissions were met when the stove was fueled with either 550 g or 600 g of pellets. High-power thermal efficiency fell within Tier 2 for both fueling conditions. Low power specific fuel consumption fell within Tier 3.

Figure 18. The P2 prototype was a field-ready unit that would be suitable for pilot testing with potential consumers.

Table 2. Laboratory performance of the P2 prototype in terms of the 2012 ISO IWA tiers.[11] Results are shown as the mean ± one standard deviation. The mean value of each metric was used to select the associated tier rating. Indoor emissions are for high-power operation, which resulted in higher emissions.

	600 g pellets		550 g pellets	
Metric	Result	Tier	Result	Tier
Time to boil (minutes)	27 ± 2	-	33 ± 2	-
High-power thermal efficiency (%)	25.6 ± 0.2	2	25.3 ± 0.4	2
High-power CO ($g \cdot MJ_d^{-1}$)	0.96 ± 0.10	4	0.84 ± 0.04	4
High-power $PM_{2.5}$ ($g \cdot MJ_d^{-1}$)	53 ± 6	3	41 ± 5	4
Low-power specific fuel consumption ($MJ \cdot min^{-1} \cdot L^{-1}$)	0.022 ± 0.003	3	-	-
Low-power CO ($g \cdot min^{-1} \cdot L^{-1}$)	0.011 ± 0.004	4	-	-
Low-power $PM_{2.5}$ ($mg \cdot min^{-1} \cdot L^{-1}$)	0.19 ± 0.05	4	-	-
Indoor emissions CO ($g \cdot min^{-1}$)	0.06 ± 0.01	4	0.043 ± 0.002	4
Indoor emissions $PM_{2.5}$ ($mg \cdot min^{-1}$)	3 ± 0.3	3	2 ± 0.4	4

Envirofit India was provided with a P2 prototype to evaluate the design and obtain customer feedback on usability. Future work will include improving high-power thermal efficiency and low power specific fuel consumption. The design would also benefit from further exploration

of the effects of combustion chamber diameter of power output and emissions. In addition, the microcontroller could be used to optimize the fan speed (and the resulting primary and secondary air flow rates) based on measured temperatures and pressures inside the plenum. Dynamic feedback between the plenum pressure and temperature and the fane speed could help improve performance of the stove during transient operating conditions without requiring input from the user.

For more information, see the following documents:

- Tillotson, J. Master's Thesis, Colorado State University, Fort Collins, CO, 2018.

REFERENCES

(1) Reed, T. B.; Larson, R. A Wood-Gas Stove for Developing Countries. *Energy Sustain. Dev.* **1996**, *3* (2), 34–37 DOI: 10.1016/S0973-0826(08)60589-X.

(2) Tryner, J. Combustion Phenomena in Biomass Gasifier Cookstoves. Ph.D. Dissertation, Colorado State University: Fort Collins, CO, 2016.

(3) Jetter, J. J.; Kariher, P. Solid-Fuel Household Cook Stoves: Characterization of Performance and Emissions. *Biomass Bioenergy* **2009**, *33* (2), 294–305 DOI: 10.1016/j.biombioe.2008.05.014.

(4) MacCarty, N.; Still, D.; Ogle, D. Fuel Use and Emissions Performance of Fifty Cooking Stoves in the Laboratory and Related Benchmarks of Performance. *Energy Sustain. Dev.* **2010**, *14* (3), 161–171 DOI: 10.1016/j.esd.2010.06.002.

(5) Jetter, J.; Zhao, Y.; Smith, K. R.; Khan, B.; Yelverton, T.; DeCarlo, P.; Hays, M. D. Pollutant Emissions and Energy Efficiency under Controlled Conditions for Household Biomass Cookstoves and Implications for Metrics Useful in Setting International Test Standards. *Environ. Sci. Technol.* **2012**, *46* (19), 10827–10834 DOI: 10.1021/es301693f.

(6) Kar, A.; Rehman, I. H.; Burney, J.; Puppala, S. P.; Suresh, R.; Singh, L.; Singh, V. K.; Ahmed, T.; Ramanathan, N.; Ramanathan, V. Real-Time Assessment of Black Carbon Pollution in Indian Households Due to Traditional and Improved Biomass Cookstoves. *Environ. Sci. Technol.* **2012**, *46* (5), 2993–3000 DOI: 10.1021/es203388g.

(7) Singh, S.; Gupta, G. P.; Kumar, B.; Kulshrestha, U. C. Comparative Study of Indoor Air Pollution Using Traditional and Improved Cooking Stoves in Rural Households of Northern India. *Energy Sustain. Dev.* **2014**, *19*, 1–6 DOI: 10.1016/j.esd.2014.01.007.

(8) Sambandam, S.; Balakrishnan, K.; Ghosh, S.; Sadasivam, A.; Madhav, S.; Ramasamy, R.; Samanta, M.; Mukhopadhyay, K.; Rehman, H.; Ramanathan, V. Can Currently Available Advanced Combustion Biomass Cook-Stoves Provide Health Relevant Exposure Reductions? Results from Initial Assessment of Select Commercial Models in India. *EcoHealth* **2015**, *12* (1), 25–41 DOI: 10.1007/s10393-014-0976-1.

(9) Tryner, J.; Willson, B. D.; Marchese, A. J. The Effects of Fuel Type and Stove Design on Emissions and Efficiency of Natural-Draft Semi-Gasifier Biomass Cookstoves. *Energy Sustain. Dev.* **2014**, *23*, 99–109 DOI: 10.1016/j.esd.2014.07.009.

(10) Tryner, J.; Tillotson, J. W.; Baumgardner, M. E.; Mohr, J. T.; DeFoort, M. W.; Marchese, A. J. The Effects of Air Flow Rates, Secondary Air Inlet Geometry, Fuel Type, and

Operating Mode on the Performance of Gasifier Cookstoves. *Environ. Sci. Technol.* **2016**, *50* (17), 9754–9763 DOI: 10.1021/acs.est.6b00440.
(11) ISO IWA 11:2012 Guidelines for evaluating cookstove performance http://cleancookstoves.org/resources_files/iso-iwa-cookstoves.pdf (accessed Jan 6, 2017).
(12) Tryner, J.; Volckens, J.; Marchese, A. J. Effects of Operational Mode on Particle Size and Number Emissions from a Biomass Gasifier Cookstove. *Aerosol Sci. Technol.* **2018**, *52* (1), 87–97 DOI: 10.1080/02786826.2017.1380779.
(13) Hardalupas, Y.; Orain, M. Local Measurements of the Time-Dependent Heat Release Rate and Equivalence Ratio Using Chemiluminescent Emission from a Flame. *Combust. Flame* **2004**, *139* (3), 188–207 DOI: 10.1016/j.combustflame.2004.08.003.
(14) Steinberg, A. M.; Boxx, I.; Stöhr, M.; Carter, C. D.; Meier, W. Flow–flame Interactions Causing Acoustically Coupled Heat Release Fluctuations in a Thermo-Acoustically Unstable Gas Turbine Model Combustor. *Combust. Flame* **2010**, *157* (12), 2250–2266 DOI: 10.1016/j.combustflame.2010.07.011.
(15) Marchese, A. J.; Dryer, F. L.; Nayagam, V.; Colantonio, R. O. Hydroxyl Radical Chemiluminescence Imaging and the Structure of Microgravity Droplet Flames. *Symp. Int. Combust.* **1996**, *26* (1), 1219–1226 DOI: 10.1016/S0082-0784(96)80338-9.
(16) Stöhr, M.; Arndt, C. M.; Meier, W. Transient Effects of Fuel–air Mixing in a Partially-Premixed Turbulent Swirl Flame. *Proc. Combust. Inst.* **2015**, *35* (3), 3327–3335 DOI: 10.1016/j.proci.2014.06.095.
(17) Lozano, A.; Yip, B.; Hanson, R. K. Acetone: A Tracer for Concentration Measurements in Gaseous Flows by Planar Laser-Induced Fluorescence. *Exp. Fluids* **1992**, *13* (6), 369–376 DOI: 10.1007/BF00223244.
(18) Sadanandan, R.; Stöhr, M.; Meier, W. Simultaneous OH-PLIF and PIV Measurements in a Gas Turbine Model Combustor. *Appl. Phys. B* **2008**, *90* (3–4), 609–618 DOI: 10.1007/s00340-007-2928-8.
(19) Denshchikov, V. A.; Kondrat'ev, V. N.; Romashov, A. N. Interaction between Two Opposed Jets. *Fluid Dyn.* **1978**, *13* (6), 924–926 DOI: 10.1007/BF01050971.
(20) Denshchikov, V. A.; Kondrat'ev, V. N.; Romashov, A. N.; Chubarov, V. M. Auto-Oscillations of Planar Colliding Jets. *Fluid Dyn.* **1983**, *18* (3), 460–462 DOI: 10.1007/BF01090570.
(21) Besbes, S.; Mhiri, H.; Le Palec, G.; Bournot, P. Numerical and Experimental Study of Two Turbulent Opposed Plane Jets. *Heat Mass Transf.* **2003**, *39* (8–9), 675–686 DOI: 10.1007/s00231-002-0336-5.
(22) Li, W.-F.; Yao, T.-L.; Liu, H.-F.; Wang, F.-C. Experimental Investigation of Flow Regimes of Axisymmetric and Planar Opposed Jets. *AIChE J.* **2011**, *57* (6), 1434–1445 DOI: 10.1002/aic.12369.
(23) Tu, G.; Li, W.; Du, K.; Huang, G.; Wang, F. Onset and Influencing Factors of Deflecting Oscillation in Planar Opposed Jets. *Chem. Eng. J.* **2014**, *247*, 125–133 DOI: 10.1016/j.cej.2014.02.097.
(24) Pawlowski, R. P.; Salinger, A. G.; Shadid, J. N.; Mountziaris, T. J. Bifurcation and Stability Analysis of Laminar Isothermal Counterflowing Jets. *J. Fluid Mech.* **2006**, *551* (1), 117 DOI: 10.1017/S0022112005008396.
(25) Barad, M.; Colella, P. A Fourth-Order Accurate Local Refinement Method for Poisson's Equation. *J. Comput. Phys.* **2005**, *209* (1), 1–18 DOI: 10.1016/j.jcp.2005.02.027.

(26) Gordon, S.; McBride, B. J. *Computer Program for Calculation of Complex Chemical Equilibrium Compositions and Applications I. Analysis*; NASA Reference Publication 1311; NASA Lewis Research Center: Cleveland, OH, 1994.
(27) Gordon, S.; McBride, B. J. *Computer Program for Calculation of Complex Chemical Equilibrium Compositions and Applications II. Users Manual and Program Description*; NASA Reference Publication 1311; NASA Lewis Research Center: Cleveland, OH, 1996; p 184.
(28) Mathur, S.; Tondon, P. K.; Saxena, S. C. Thermal Conductivity of Binary, Ternary and Quaternary Mixtures of Rare Gases. *Mol. Phys.* **1967**, *12* (6), 569–579 DOI: 10.1080/00268976700100731.
(29) Anderson, Jr., J. D. *Hypersonic and High Temperature Gas Dynamics*, 1st ed.; McGraw-Hill: New York, 1989.
(30) Yee, H. .; Sandham, N. .; Djomehri, M. . Low-Dissipative High-Order Shock-Capturing Methods Using Characteristic-Based Filters. *J. Comput. Phys.* **1999**, *150* (1), 199–238 DOI: 10.1006/jcph.1998.6177.
(31) Guzik, S. M.; Gao, X.; Owen, L. D.; McCorquodale, P.; Colella, P. A Freestream-Preserving Fourth-Order Finite-Volume Method in Mapped Coordinates with Adaptive-Mesh Refinement. *Comput. Fluids* **2015**, *123*, 202–217 DOI: 10.1016/j.compfluid.2015.10.001.
(32) Attal, N.; Ramaprabhu, P.; Hossain, J.; Karkhanis, V.; Uddin, M.; Gord, J. R.; Roy, S. Development and Validation of a Chemical Reaction Solver Coupled to the FLASH Code for Combustion Applications. *Comput. Fluids* **2015**, *107*, 59–76 DOI: 10.1016/j.compfluid.2014.09.051.
(33) Wilke, C. R. A Viscosity Equation for Gas Mixtures. *J. Chem. Phys.* **1950**, *18* (4), 517–519 DOI: 10.1063/1.1747673.
(34) Burke, M. P.; Chaos, M.; Ju, Y.; Dryer, F. L.; Klippenstein, S. J. Comprehensive H_2/O_2 Kinetic Model for High-Pressure Combustion. *Int. J. Chem. Kinet.* **2012**, *44* (7), 444–474 DOI: 10.1002/kin.20603.
(35) Kéromnès, A.; Metcalfe, W. K.; Heufer, K. A.; Donohoe, N.; Das, A. K.; Sung, C.-J.; Herzler, J.; Naumann, C.; Griebel, P.; Mathieu, O.; Krejci, M. C.; Petersen, E. L.; Pitz, W. J.; Curran, H. J. An Experimental and Detailed Chemical Kinetic Modeling Study of Hydrogen and Syngas Mixture Oxidation at Elevated Pressures. *Combust. Flame* **2013**, *160* (6), 995–1011 DOI: 10.1016/j.combustflame.2013.01.001.
(36) Haas, F. M. Studies of Small Molecule Reactions Foundational to Combustion Chemistry, Including Experimental Measurements from a Novel High Pressure Flow Reactor. Ph.D. Dissertation, Princeton University: Princeton, NJ, 2016.
(37) Joshi, A. V.; Wang, H. Master Equation Modeling of Wide Range Temperature and Pressure Dependence of CO + OH → Products. *Int. J. Chem. Kinet.* **2006**, *38* (1), 57–73 DOI: 10.1002/kin.20137.
(38) Sharipov, A.; Starik, A. Theoretical Study of the Reaction of Carbon Monoxide with Oxygen Molecules in the Ground Triplet and Singlet Delta States. *J. Phys. Chem. A* **2011**, *115* (10), 1795–1803 DOI: 10.1021/jp110345s.
(39) Jasper, A. W.; Dawes, R. Non-Born–Oppenheimer Molecular Dynamics of the Spin-Forbidden Reaction $O(^3P) + CO(X^1\Sigma^+) \rightarrow CO_2(\tilde{X}^1\Sigma_g^+)$. *J. Chem. Phys.* **2013**, *139* (15), 154313 DOI: 10.1063/1.4825204.
(40) Li, J.; Zhao, Z.; Kazakov, A.; Chaos, M.; Dryer, F. L.; Scire, J. J. A Comprehensive Kinetic Mechanism for CO, CH_2O, and CH_3OH Combustion: Comprehensive Kinetic

Mechanism for CO, CH_2O, and CH_3OH Combustion. *Int. J. Chem. Kinet.* **2007**, *39* (3), 109–136 DOI: 10.1002/kin.20218.

(41) Harding, L. B.; Wagner, A. F. The Reaction of Atomic Hydrogen with the Formyl Radical. *Symp. Int. Combust.* **1988**, *21* (1), 721–728 DOI: 10.1016/S0082-0784(88)80304-7.

(42) Goos, E.; Burcat, A.; Ruscic, B. Ideal gas thermochemical database with updates from Active Thermochemical Tables ftp://ftp.technion.ac.il/pub/supported/aetdd /thermodynamics.

(43) Burcat, A.; Ruscic, B. *Third Millennium Ideal Gas and Condensed Phase Thermochemical Database for Combustion with Updates from Active Thermochemical Tables*; ANL-05/20; Argonne National Laboratory and Technion-Israel Institute of Technology: Argonne, IL, 2005.

(44) Ruscic, B.; Pinzon, R. E.; Morton, M. L.; von Laszevski, G.; Bittner, S. J.; Nijsure, S. G.; Amin, K. A.; Minkoff, M.; Wagner, A. F. Introduction to Active Thermochemical Tables: Several "Key" Enthalpies of Formation Revisited. *J. Phys. Chem. A* **2004**, *108* (45), 9979–9997 DOI: 10.1021/jp047912y.

(45) Wang, H.; You, X.; Joshi, A. V.; Davis, S. G.; Laskin, A.; Egolfopoulos, F.; Law, C. K. USC Mech Version II. High-Temperature Combustion Reaction Model of $H_2/CO/C_1$-C_4 Compounds. May 2007.

(46) Paul, P.; Warnatz, J. A Re-Evaluation of the Means Used to Calculate Transport Properties of Reacting Flows. *Symp. Int. Combust.* **1998**, *27* (1), 495–504 DOI: 10.1016/S0082-0784(98)80439-6.

(47) Kee, R.; Rupley, F.; Miller, J.; Coltrin, M.; Grcar, J.; Meeks, E. *Chemkin Collection, Release 3.7.1*; Reaction Design Inc.: San Diego, CA, 2003.

(48) Dean, A. M.; Steiner, D. C.; Wang, E. E. A Shock Tube Study of the $H_2/O_2/CO/Ar$ and $H_2/N_2O/CO/Ar$ Systems: Measurement of the Rate Constant for $H + N_2O = N_2 + OH$. *Combust. Flame* **1978**, *32*, 73–83 DOI: 10.1016/0010-2180(78)90081-0.

(49) Sun, H.; Yang, S. I.; Jomaas, G.; Law, C. K. High-Pressure Laminar Flame Speeds and Kinetic Modeling of Carbon Monoxide/Hydrogen Combustion. *Proc. Combust. Inst.* **2007**, *31* (1), 439–446 DOI: 10.1016/j.proci.2006.07.193.

(50) Yetter, R. A.; Dryer, F. L.; Rabitz, H. Flow Reactor Studies of Carbon Monoxide/Hydrogen/Oxygen Kinetics. *Combust. Sci. Technol.* **1991**, *79* (1–3), 129–140 DOI: 10.1080/00102209108951760.